PAPER

Check for updates

Multifunctional ternary ZnMgFe LDH as an efficient adsorbent for ceftriaxone sodium and antimicrobial agent: sustainability of adsorption waste as a catalyst for methanol electro-oxidation

Hala Mohamed,[a] Rehab Mahmoud,[b] Abdalla Abdelwahab, [ID][ca] Ahmed A. Farghali,[a] Fatma I. Abo El-Ela [ID][d] and Abeer Enaiet Allah [ID]*[b]

In order to achieve sustainable benefits for the adsorption of wastewater pollutants, spent adsorbents need to be recycled and/or valorized. This work studied a two-dimensional (2D) ZnMgFe layered double hydroxide (LDH) for ceftriaxone sodium (CTX) adsorption. This LDH showed a crystallite size of 9.8 nm, a BET surface area of 367.59 m^2 g^{-1}, and a micro-sphere-like morphology. The factors investigated in this study were the adsorbent dose, initial concentration, initial pH, and contact time. ZnMgFe LDH showed 99% removal of CTX with a maximum adsorption capacity of 241.75 mg g^{-1} at pH = 5. The Dubinin−Radushkevich model was found to be the most adequate isotherm model. The spent adsorbent (ZnMgFe LDH/CTX) was reused as an electro-oxidation catalyst for direct methanol fuel cells. ZnMgFe LDH/CTX showed almost a 10-fold increase in electrochemical activity for all scan rates compared to bare ZnMgFe LDH in 1 M KOH. As methanol concentration increases, the maximum current density generated by both the ZnMgFe LDH and ZnMgFe LDH/CTX samples increases. Moreover, the maximum current density for ZnMgFe LDH/CTX was 47 mA cm^{-2} at a methanol concentration of 3 M. Both samples possess reasonable stability over a 3600 S time window with no significant deterioration of electrochemical performance. Moreover, the antimicrobial studies showed that ZnMgFe LDH had a significant antifungal (especially *Aspergillus*, *Mucor*, and Penicillium species) and antibacterial (with greater action against Gram-positive than negative) impact on several severe infectious diseases, including *Aspergillus*. This study paves the way for the reuse and valorization of selected adsorbents toward circular economy requirements.

1. Introduction

Chemical and biochemical industrial processes have caused the discharge of numerous potential emerging pollutants (PEPs) in wastewater effluents. PEPs are classified as hazardous materials by the United States Environmental Protection Agency.[1] Conventional wastewater treatment plants cannot handle the existence of such emerging pollutants in wastewater feed streams.[2] Several technologies are under investigation for the treatment of such contaminated wastewater streams including adsorption. Adsorption can be defined as the accumulation of a pollutant (adsorbate) onto the surface of adsorbents for the purpose of separation from a medium.[3] Several conventional

and nano-adsorbents have been recognized as considerable candidates for the separation of PEPs from wastewater samples. One of the promising 2D nano-adsorbents under investigation is layered double hydroxides (LDHs). LDHs are defined as 2D anionic clay materials, similar in structure to brucite, which possess the chemical formula $[M(II)_{(1-x)}M(III)_x(OH)_2]^{x+}(A^{n-})_{x/n} \cdot yH_2O$. $M(II)$ is a divalent cation such as Mg, Cu, or Co while $M(III)$ is a trivalent cation such as Al, Cr, or Fe, and A^{n-} represents the negative anions such as CO_3^{-2}, Cl^-, and NO_3^-.[4] LDHs have attracted much interest as adsorbents due to their adequate specific surface area, low toxicity, high removal capacity, simple recoverability procedures, cost-effective synthesis, and stable physicochemical properties.[5]

On the other hand, finding a promising nano-adsorbent is not enough to achieve a sustainable and cost-effective large-scale adsorption process. Achieving circular economy principles requires further investigations to modify, reuse and valorize spent adsorbents that can no longer be regenerated.[6,7] Currently, the strategy of reusing spent adsorbents became an important field of research. Recently, Baskar *et al.*[8] illustrated

[a]Department of Materials Science and Nanotechnology, Faculty of Postgraduate Studies for Advanced Sciences, Beni-Suef University, Beni-Suef 62511, Egypt

[b]Chemistry Department, Faculty of Science, Beni-Suef University, 62511, Egypt. E-mail: abeer.abdelaal@science.bsu.edu.eg

[c]Faculty of Science, Galala University, Sokhna 43511, Suez, Egypt

[d]Department of Pharmacology, Faculty of Veterinary Medicine, Beni-Suef University, 62511, Egypt

the different approaches for the re-utilization of spent adsorbents. One strategy to valorize spent adsorbents is re-incorporating them into different applications and/or technologies such as catalysis, super-capacitors, (bio)sensors, composite-fillers, and additives. One particular application, methanol electro-oxidation, is a promising route to valorize spend adsorbents. Methanol is a promising fuel that can be oxidized in a direct methanol fuel cell to produce carbon dioxide and water as oxidation products.[9] At the anode, water and methanol are consumed to produce protons, electrons, and carbon dioxide. The electrons flow in an external circuit and reach the cathode to reduce oxygen. Numerous nanomaterials were investigated as anode materials that can efficiently catalyze the methanol consumption reaction.[10–12] Investigating spent adsorbents as methanol fuel cell anodes is a novel field of research, which can lead to producing cheap and effective anode materials. This can lead to improving the performance and decrease the cost of direct alcohol fuel cells in the future.

Based on the aforementioned aspects, this study devoted particular attention to the valorization of the waste material after drug adsorption, the protection of the environment, and energy production in an innovative concept for a multi-functional LDH structure. Few studies, in the open literature, report the reuse of spent LDH after adsorption. Our research group has contributed to this field by investigating novel techniques to reuse and/or valorize spent LDH-based nano-adsorbents. Abdel-Hady *et al.*[13] prepared ZnCoFe LDH using a simple co-precipitation-based method. The synthesized ZnCoFe LDH was used as a nano-adsorbent for methylene blue (MB) adsorption. The adsorbent showed a removal percent of 88.6% at pH 7, 100 mg L^{-1} MB concentration, and 0.1 g of LDH. The spent adsorbent was analyzed as a direct methanol electro-oxidation (DMEO) catalyst. The study showed a maximum current density of 41.11 mA cm^{-2} at methanol concentration =

3 M and 50 mV s^{-1} scan rate. In another study, Abdel-Hady *et al.*[14] synthesized double substituted NiCo–ZnFe LDH, which was calcined at 200 °C, 400 °C, and 600 °C. The NiCo–ZnFe LDH adsorbent and the resultant mixed metal oxides (MMO) after calcination were used for the adsorption of methyl orange (MO). The spent adsorbents (after MO adsorption) were reused as electro-catalysts for DMEO, the samples showed a maximum current density of 6.46 and 10.1 mA cm^{-2} for the LDH and MMO (calcined at 200 °C) respectively. Kamal *et al.*[15] prepared CoZnFe LDH for oxytetracycline (OTC) adsorption showing an adsorption capacity of 240.29 mg g^{-1} (100% removal percentage). The spent adsorbent was used for DMEO and showed a maximum current density of approximately 18 mA cm^{-2} in 0.74 M methanol and 60 mV s^{-1} scan rate.

Additionally, the incidence of fungal musculoskeletal diseases in animals and humans, particularly those infected by wastewater, makes water disinfection applications crucial. *Candida* is frequent. *Candida albicans* is a soil-dwelling human commensal. *Aspergillus* bone and joint infections have a poor prognosis and neurological complications. Immunosuppression, intravenous drugs, chronic illnesses, and surgery predispose hosts. Polluted air or water pipes might transmit nosocomial diseases. The most frequent pathogen is *Aspergillus fumigatus*, followed by *A. Flavus* and *A. Niger*. Targeted and personalized antifungal treatment is needed.[16] Gram-positive and Gram-negative microorganisms cause a minority of bone and joint infections. Before the Hib immunization, *Haemophilus influenza* caused septic arthritic joints in pre-schoolers.[17] So water sanitation is a critical issue for the prevention of serious infective diseases in both animals and humans.

The aim of the current work is to prepare, characterize and investigate multifunctional ZnMgFe LDH as a 2D nano-adsorbent for ceftriaxone sodium (CTX) adsorption from simulated wastewater. The effects of solution pH, adsorbent
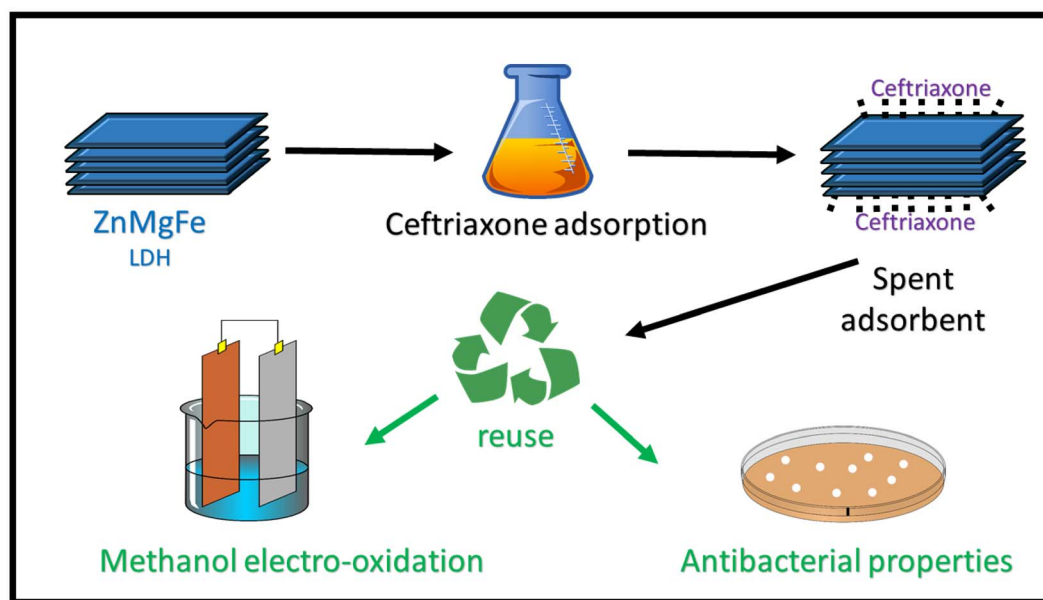
Scheme 1 The procedure of reusing ZnMgFe LDH spent adsorbent for DMEO.

dosage, adsorbate initial concentration, adsorption kinetics, and operating temperature were studied. The spent adsorbent was further valorized as an electro-catalyst for DMEO. In addition, the nano adsorbent was also investigated as a potential antimicrobial agent against both bacterial and fungal infections, which can be used for water disinfection and/or antimicrobial applications. The aim of this work is illustrated in Scheme 1.

2. Materials and methods

2.1 Materials

Zinc nitrate (Chem-Lab NV – Belgium), magnesium, and ferric nitrates (Oxford – India) were used as received without further purification. Sodium hydroxide (NaOH) was supplied by Egyptian Piochem for laboratory chemicals. Hydrochloric acid (HCl) was purchased from CarloErba reagents (Egypt). Methanol was purchased from ALPHA CHEMIKA-India.

This study used fungal isolates from the Fungal Research Institute (Doki, Giza, Cairo) reference collection and bacterial strains from the ATCC at the Cairo Microbiology Research Center. Phylogenetic reconstruction included therapeutically important *Mucorales* taxa. CNRMA03894 Indicus Human muscle and bone affected each other in this investigation. Cycloheximide was the antifungal standard, while Pharma Swede Pharmaceutical Company provided doxorubicin. Antibacterial studies used Gram-positive *S. pneumonia*, *S. aureus*, *Listeria monocytogenes*, *E. coli*, *Haemophilus influenza*, and *Bacillus subtlis* (ATCC 35021). Regional Centre for Mycology and Biotechnology (RCMB) isolates for Aspergillosis included *Aspergillus flavus* RCMB 02783, *Fumigatus* RCMB 02564, and *Niger* RCMB 02588, Candidacies (*Candida albicans* RCMB 05035), Mucormycosis (*M. indicus* CNRMA 03.894), and *Penicillium notatum* (NCPF 2881). Muller Hinton broth and agar were used to culture several bacterial strains in an incubator at 37 °C for 24 h. The temperature was kept at 25 °C for five days while Sabaroud dextrose agar and broth were used for fungal growth with cycloheximide. Each tube was autoclaved before experimentation.

2.2 Synthesis of ZnMgFe LDH

ZnMgFe LDH was prepared by a facile co-precipitation technique following a Zn : Mg : Fe molar ratio of 2 : 2 : 1. $Zn(NO_3)_2 \cdot 6H_2O$, $Mg(NO_3)_2 \cdot 6H_2O$ and $Fe(NO_3)_3 \cdot 9H_2O$ were dissolved in 500 mL of distilled water. 2 M of NaOH solution was, drop wisely, and added until the pH reached 10 at 60 °C. Then this suspension was stirred for 24 h. After that, the formed precipitate was collected by centrifuge and repeatedly rinsed with distilled H_2O to remove any remaining NaOH (*i.e.*, pH = 7), then dried at 80 °C for 12 h. The final precipitate was subsequently ground to uniform particle size.

2.3 Material characterization

The prepared ZnMgFe LDH was characterized using different tools: PANalytical (Empyrean) X-ray diffractometer with Cu-Kα radiation (wavelength 0.154 nm, $I = 35$ mA, $V = 40$ kV, scanning

at a rate of 8° min^{-1}) from two-theta of 5° to 80° was used to determine the crystallinity of the sample. The functional groups were determined using Fourier transform infrared (FTIR) spectroscopy (Bruker-Vertex 70, KBr pellet technique, Germany), from 400 to 4000 cm^{-1} wavenumber. The morphology of the synthesized ZnMgFe LDH was investigated using Field Emission Scanning Electron Microscope (FESEM). CTX concentrations were tracked using a UV-vis spectrophotometer (SHIMADZU UV-2600). The pH of the solution was determined using an (A∂wa–AD1030) pH meter, on Malvern zeta sizer equipment, hydrodynamic particle sizes, and zeta potential were measured (Malvern instruments Ltd), an automatic surface area Braeuer–Emmett–Teller (BET), specific pore volume and pore diameters were measured using (TriStar II 3020, Micromeritics, USA) nitrogen adsorption–desorption isotherm. Thermal stability and phase transition of the prepared materials were investigated utilizing TGA/DTA instrument.

2.4 Adsorption study

The adsorption experiments were performed in a batch mode at room temperature (25 °C). A 1000 mg CTX/L stock solution was prepared to allow for serial dilution. To study the effect of pH, 50 mL Falcon tubes were used with 0.05 g of the synthesized ZnMgFe LDH adsorbent. The pH, which was measured by pH meter (Metrohm 751 Titrino), was adjusted to the required value by 0.1 M NaOH or 0.1 M HCl solutions. An orbital shaker was used for shaking the samples overnight. Liquid wastewater samples were collected using a syringe equipped with a syringe filter (Millipore, Nylon, 0.22 mm pore size). The residual concentration of CTX was measured using UV-vis spectroscopy.

The quantity of CTX adsorbed (q_e) and removal percentage (% RE) were calculated according to eqn (1) and (2) respectively:

$$q_e = \frac{(C_o - C_t)V}{W} \tag{1}$$

$$\text{Removal percent } (\%\ \text{RE}) = \frac{C_o - C_t}{C_o} \times 100 \tag{2}$$

where q_e is the amount of CTX adsorbed per gram, C_o, and C_t are the initial concentration and the concentration after adsorption of CTX in (mg L^{-1}) at time t (min) respectively. W is the mass of ZnMgFe in grams and V is the volume of CTX solution (litre).

The effect of adsorbent dosage was investigated at a constant CTX concentration (50 mg L^{-1}) while the dose of adsorbent was varied from 0.0125 g to 0.10 g. Different CTX initial concentrations were used ranging from 5 mg L^{-1} to 500 mg L^{-1} to study the adsorption isotherms. Moreover, numerous isotherm models have been investigated to fit the adsorption data. To follow, the effect of temperature on the adsorption process was examined at 15 °C, 25 °C, 35 °C, 45 °C, and 55 °C. Then, the corresponding thermodynamic functions were calculated. Finally, CTX adsorption kinetics were investigated and then fitted to various kinetic models such as pseudo-first-order,[18] pseudo-second-order,[19] intra-particle diffusion,[20] and Avrami.[21]

The thermodynamic analysis was conducted by calculating Gibb's free energy change ($\Delta G°$), enthalpy change ($\Delta H°$), and

entropy change ($\Delta S°$). The values of $K_d = (q_e/c_e)$ were also calculated at various temperatures using Van't Hoff equation to determine the mechanism of the adsorption process.[22]

$$\ln K_d = \Delta S°/R - \Delta H°/RT \quad (3)$$

where K_d is the equilibrium constant (L mg^{-1}), $\Delta H°$ is the enthalpy change of adsorption (kJ mol^{-1}), R is the gas constant (8.314 J mol^{-1} K^{-1}), and $\Delta S°$ is the entropy change of adsorption. Gibbs free energy change ($\Delta G°$) could be calculated using eqn (4) and (5).

$$\Delta G° = -RT \ln K_d = \Delta H° - T\Delta S° \quad (4)$$

$$\ln K_d = -\Delta H°/R(1/T) + \Delta S°/R \quad (5)$$

2.5 Electrochemical methanol oxidation using the spent ZnMgFe LDH

The spent LDH powder was collected after adsorption, washed then dried for 24 h at 80 °C. The effective working electrode modification for oxidizing methanol relied on using a glassy carbon electrode (GCE), which has a 3 mm diameter and was polished with fine alumina powder before use. Then, a slurry containing 5 mg of spent ZnMgFe LDH in 400 μL of isopropanol and 15 μL of a 5% Nafion solution was sonicated at room temperature for 30 minutes. Then, 10 μL of the sonicated suspension was poured over the GC electrode's active region. To follow, the electrode surface was dried for a final 30 minutes at 60 °C.

Electrocatalytic activity of ZnMgFe LDH and ZnMgFe LDH/CTX was measured utilizing a potentiostat/galvanostat (AUTOLAB PGSTAT 302N, Metrohm, Herisau, Switzerland) with NOVA 1.11 software. Conventional three-compartment glass cell with a counter electrode of Pt wire, GC, and Ag/AgCl as the reference electrode was used. To assess the electrocatalytic activity of the produced electrodes, a 1 M KOH electrolyte solution with and without methanol was utilized. Scanning rates ranging from 5 mV to 60 mV were used for the cyclic voltammetry experiments. The chronoamperometry (CA) measurements lasted 3600 seconds at 0.6 V. Total organic carbon was measured on Teledyne-Tekmar, TOC Fusion, Model 14-9600-200 (USA).

2.6 Estimation of the antimicrobial activity of spent ZnMgFe LDH

2.6.1 Fungal isolates and bacterial inoculum preparations.
Recent cultures of *Aspergillus flavus*, *Fumigatus*, *Niger*, *Candida albicans*, *M. indicus* CNRMA 03.894, and *Penicillium notatum* (NCPF 2881) was used to make suspensions, which were plated on Sabouraud's dextrose agar (SDA). After incubation, 4–5 yeast colonies were transferred to test tubes with 5 mL of 0.9% saline solution using a sterile loop. A suspension of barium sulfates 1.175% and sulphuric acid 1% standardized the final inoculum's turbidity (turbidity or standard tube, McFarland 0.5). It was 1.5×10^8 CFU mL^{-1}.[23] To create bacterial inoculum, *S. pneumonia*, *S. aureus*, *Listeria monocytogenes* as Gram positive

strains, while Gram-negative *E. coli*, *Haemophillus influenza*, and *Bacillus subtlis* were plated on Muller Hinton agar medium and incubated at 37 °C for 24 h. After incubation, around six colonies were submerged in saline by traditional tube matching to yield 10^8 CFU mL^{-1}, as described in fungal inoculum preparation.

2.6.2 Minimal inhibitory concentration for bacterial isolates.
The micro-dilution susceptibility test in Muller–Hinton broth (Oxoid) and Sabouraud's liquid medium (Oxoid) was used to estimate the MIC for bacteria and fungus, respectively. Chemical solutions were stock tested in saline. Standard technique broth diluted the stock solution (Difco). Twofold serial dilutions of the broth with 10^8 CFU mL^{-1} test microorganisms are produced. Each 96-well microtiter plate well received the solution. Microplates were sealed and incubated at 37 °C in a humid environment for 24 hours to achieve antibacterial activity. The MIC values were the lowest chemical concentrations that did not generate apparent turbidity before incubation. An uninoculated medium was the control in investigations using the test compounds. Each experiment was repeated three times for repeatability. SPSS version 21 generated means and SD values, and P values less than 0.05 were statistically significant.

2.6.3 Minimal bactericidal concentration (MBC).
The MIC dilution and at least two additional concentrated ZnMgFe LDH dilutions are plated on Muller Hinton agar plate to assess viable CFU mL^{-1}. MBC is the lowest ZnMgFe LDH concentration that does not produce viable bacterial colonies after 24 h at 37 °C (bactericidal activity).

2.6.4 Minimum inhibitory concentration for fungal isolates (MIC-f).
Fungi MIC determination using broth microdilution.[23] A "U"-bottomed 96-well microdilution plate received 100 μL of Sabouraud's dextrose broth medium (SDB). The first horizontal row of plate wells received 100 μL of the tested nanomaterials emulsion. Concentrations ranged from 1000 to 1.9 μg mL^{-1} after transferring a 100 μL aliquot from the most concentrated well to the next. Each column of the plate received 10 μL of an inoculum suspension comprising various strains. A positive control (medium without fungal strains) and a negative control (medium without materials and fungal strains) were cultivated in cycloheximide (media with the fungi but without nanomaterials). Each well of SDB plates contained 100 μL of SDB with varied nanomaterial concentrations in 2-fold serial dilutions (1000, 500, 250, 125, 62.5, 31.25, 15.62, 7.81, 3.95, and 1.95 μg mL^{-1}). After dilution, 1.5×10^8 fungal strains per mL, 10 μL solutions were injected 72 hours at 25 °C incubated U-shaped plates. The growth was visually assessed after incubation. Plate well cell clusters or "buttons" were considered. The lowest concentration that noticeably reduced fungal growth was the MIC. Morales *et al.* assessed the nanoparticles' antibacterial activity (considered active or inactive):[21] strong/excellent activity (MIC < 1000 μg mL^{-1}).

2.6.5 Sorbitol assay-effect ZnMgFe LDH on the cell wall of different tested fungal strains.
The experiment examined nanomaterials' effects on fungus cell walls in sorbitol-containing and control mediums. Sorbitol at 0.8 M (5 g L^{-1}) was added to peptone water medium (15 g L^{-1}). Microdilution was performed on "U"-shaped 96-well plates. Aseptically sealed

plates were incubated at 35 degrees celsius and read on the fifth day. The increased MIC values in the medium with added sorbitol compared to the regular medium showed that ZnMgFe LDH may target the fungal cell wall due to its osmotic protective properties. Placebo was cycloheximide. The arithmetic mean of three assays was reported.[24]

2.6.6 Minimum fungicidal concentration assay (MFC). To test the MFC, we infected SDA-coated Petri plates with 100 μL aliquots of MIC, MIC 2, and MIC 4 of the nanomaterials, cycloheximide, and the fungal growth negative control. After 72 hours at 25 °C, the MFC was assessed by control organism growth. The minimum fungicidal concentration (MFC) was the lowest product concentration that inhibited fungi growth by 50 or 99.9%.[25] MIC and MFC values were averaged from triplicate biological activity assays. Both dilution approaches could verify whether the chemical is active, but they cannot indicate whether it would kill or delay the fungus. The MFC test is used for this. Depending on the fungus species, broth dilution test aliquots are subcultured on a rich solid medium and incubated for a set time and temperature. The MFC is the lowest drug concentration where no subculture growth is seen, according to CLSI-standardized publications. MFC may reveal fungicide or fungistatic activity. If the MFC and MIC are the same, the drug is a compound fungicide; if it is greater, it is fungistatic.[26]

2.6.7 Disc diffusion assay. Whatman filter paper discs were manufactured and sterilized in 10 screw-capped wide-mouthed containers for standard-size (50 mm diameter) disc diffusion examination of all tested bacteria. The bottles went through a 150 °C hot air oven. Then, sterile filter paper standard discs were impregnated with a 1000 μg mL^{-1} solution of NaTNT in saline. They were then duplicated on nutrient agar plates with the appropriate test organism. The standard antibacterial test used 10^8 CFU mL^{-1}. Two filter paper discs were infected in 12 cm Petri plates. Gram-positive *S. pneumonia*, *S. aureus*, *Listeria monocytogenes*, *E. coli*, *Haemophillus influenza*, and *Bacillus subtlis* were used as test organisms (ATCC 35021). Gram-negative, Gram-positive, and fungus were treated with doxycycline. For bacteria and fungi, plates were incubated at 37 °C for 24 hours and 25 °C for 5 days. Twofold serial dilution showed a large derivative growth inhibition zone.

2.6.8 Agar diffusion method for fungal isolates. The agar diffusion technique is a semi-quantitative assay that applies a sample with a known concentration to a Sabaroud agar surface that has been inoculated with a standard number of fungal cells (*Aspergillus flavus* RCMB 02782, *Aspergillus fumigatus* RCMB 02564, and *Aspergillus niger* RCMB 02782), *Candidacies* (*Candida albicans* RCMB 05). The sample may be administered by disc diffusion, in which 6 mm sterile filter paper discs are soaked in the sample and applied to the agar surface in the presence of cycloheximide, the standard antifungal. Samples produce a circular concentration gradient in the agar medium after inoculation. As the fungus grows around the disc, the sample's antifungal effect will limit growth. This inhibitory zone is measured in millimeters and classified as full inhibition, medium inhibition, or no inhibition by certain authors.[27,28]

2.6.9 Antifungal assay. Agar dilution for nanomaterial antifungal activity testing. Jeff-Agboola *et al.* method's,[29] after 72 hours of development on SDA at 25 degrees celsius, randomly chosen fungi were suspended in physiological saline (0.9% NaCl) and adjusted to 1.5 × 108 CFU to test ZnMgFe LDH's antifungal activity. The studied nanomaterials were prepared and blended with SDA depending on concentration after autoclaving SDA at 121 °C for 15 minutes and storing it at 55 °C. 1–3% ZnMgFe LDH was produced. Sterilized Petri plates received 20 mL of solidified Sabaroud-agar medium. Inoculating and spearing equal quantities of fungal solutions on agar media. After 72 h at 25 °C, the plates were tested on day five.

2.6.10 Statistical analysis. The mean standard deviation of the mean was shown (S.E.M.). Snedecor used a one-way analysis of variance to determine statistical significance (ANOVA),[29] SPSS (20.0) ran Tukey's post-hoc test for multiple comparisons (IBM SPSS Statistic 20.0, Armonk, NY, USA). *P* values below 0.05 were significant.

3. Results and discussion

3.1 ZnMgFe LDH characterization

The scanning electron microscope was employed to investigate the surface morphology of the prepared ZnMgFe LDH at different magnifications as shown in Fig. 1a and b. The SEM images of the prepared ZnMgFe LDH nanocomposite show layers, sheets, and microsphere-like structures, which are characteristic of LDH materials. Fig. 1a shows microspheres and cross-linked nanoflake structures, which confirm the high porosity of the prepared Zn–Fe–Mg LDH that improves the active site channel for the prepared adsorbate and enhances the adsorption capacity. The flower-like morphology and accumulation of layers presented in Fig. 1b may be due to the precipitation technique for sample preparation. This accumulation provides low crystallinity and higher surface area as it would be illustrated by the BET technique. The interlayers generated from aggregations into the LDH build channels and pits structure which facilitate the intercalation between ZnMgFe LDH and ceftriaxone. The particle size distribution was calculated to range between 250 and 430 nm. EDX analysis was conducted to confirm the presence of Zn, Fe, and Mg. Fig. 1c illustrates the EDX spectra of ZnMgFe LDH nanocomposite, which confirms the presence of Zn, Fe, and Mg with molar ratios 0.618, 1.01, and 0.12, respectively.

The Brunauer–Emmet–Teller (BET) surface area and pore size distributions of the prepared ZnMgFe LDH nanocomposite were estimated by nitrogen adsorption and desorption isotherms. According to IUPAC classification, Fig. 2a shows an isotherm of type (IV) and H3 hysteresis loop II. As a result, the ZnMgFe LDH nanocomposite contains an aggregation of particles in flat sheets with pores of non-uniform-shaped slits.[30] This H3 hysteresis loop is characteristic of microporous materials.[30] However (Fig. 2c), shows BJH pore size distributions with major pores in the mesoporous region. The results of this analysis are shown in Table 1. The BET pore volume and pore size (Fig. 2b) of the mesoporous composite were 0.6 cm^3 g^{-1} and 6.6 nm, respectively. Based on the adsorption isotherms
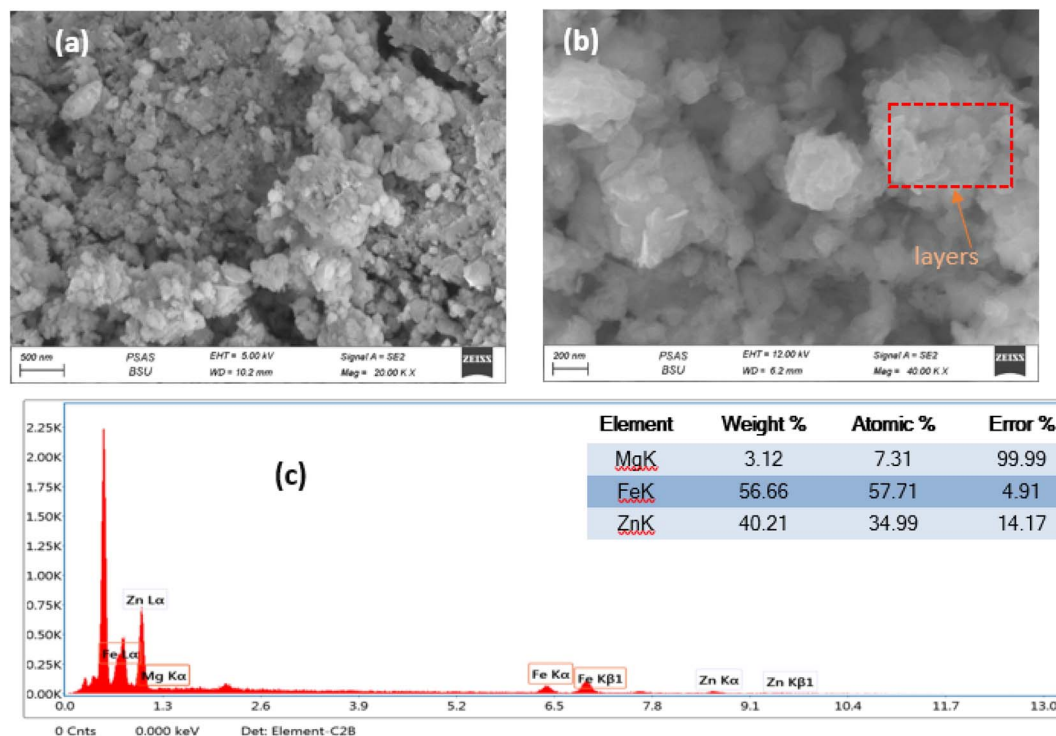
Fig. 1 (a) and (b) Scanning electron microscopy images, (c) energy-dispersive X-ray spectroscopy of synthesized ZnMgFe LDH.
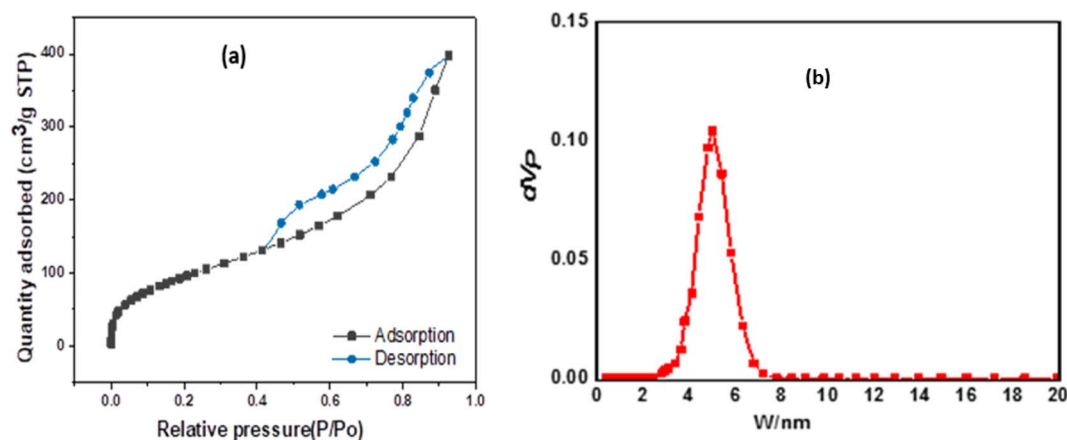

Fig. 2 (a) N_2 adsorption–desorption isotherms, (b) pore size distribution of Zn MgFe LDH composite.

measurements of the ZnMgFe LDH, a high specific surface area S_{BET} equal to 367 m^2 g^{-1} was obtained. The large surface area of the adsorbent supports the interaction between ZnMgFe LDH and CTX molecules.

XRD spectrum of prepared ZnMgFe LDH is given in Fig. 3a. It shows the characteristic diffraction peaks of LDH materials.

Table 1 Specific surface, pore volume, and average pore size of ZnMgFe LDH

Specific surface (m^2 g^{-1})	BJH pore volume (cm^3 g^{-1})	BJH pore size (nm)
367	0.616	6.69

The diffraction peaks located at 2θ of 11.2°, 22.5°, 34°, and 60° correlate with (003), (006), (009), and (011) respectively. The diffraction peaks are in good accordance with the literature values.[31] The sample has a rhombohedral crystal structure with $R\bar{3}$ space group (group number 148).[32] According to Debye–Scherrer equation, the crystallite size of ZnMgFe LDH was calculated to be 9.8 nm, and interplanar spacing for the highest peak intensity ($2\theta = 11.2$°) (003) was found to be (7.8 Å) which is close to the literature. The small diffraction intensity and noisy profile are an indication of low crystallinity, which is characteristic for LDH materials prepared by precipitation methods. Moreover, low crystalline structures with defective sites are often necessary for enhanced catalytic activities, such structures
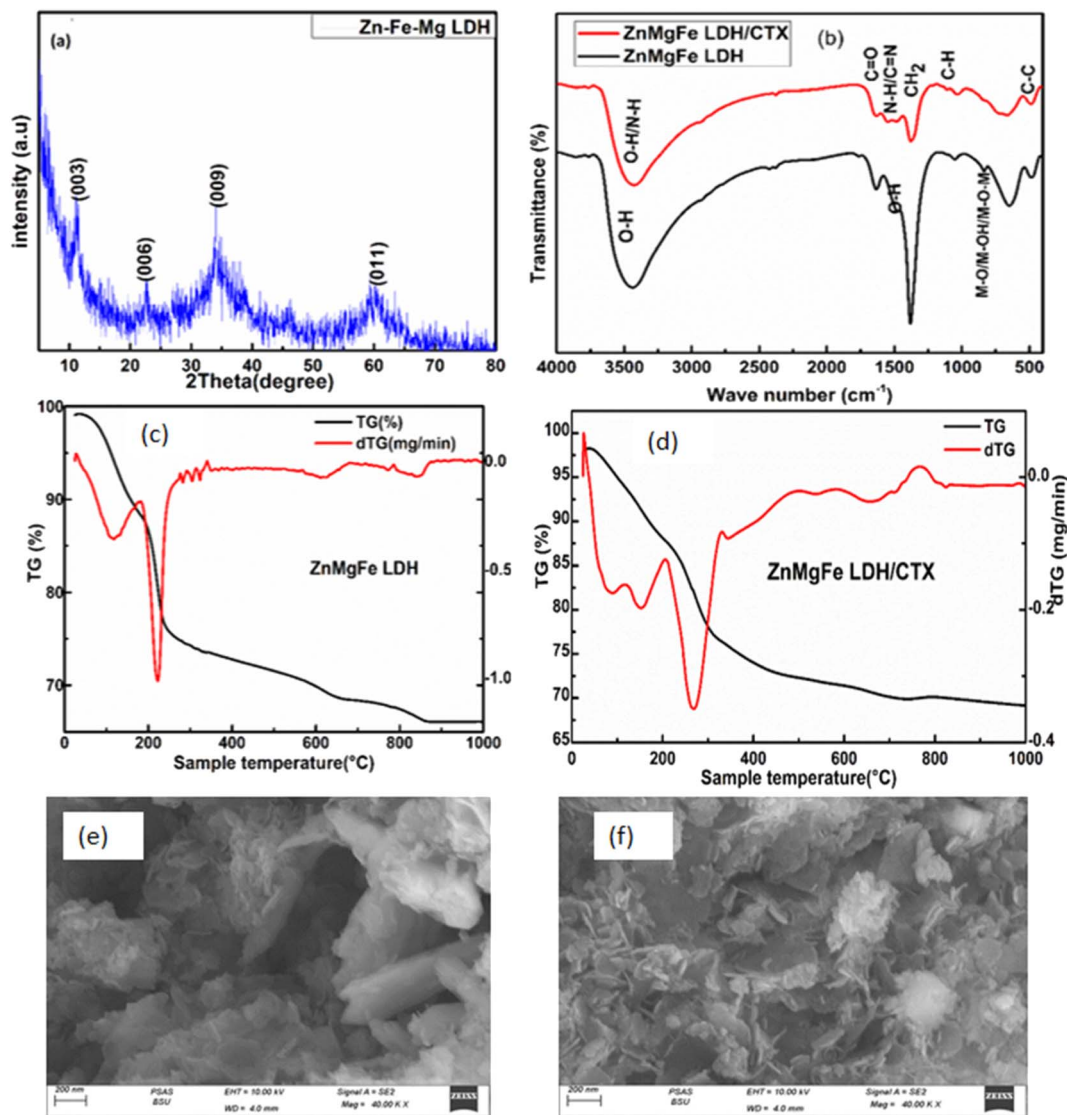
Fig. 3 (a) XRD patterns Zn–Fe–Mg LDH, (b) FTIR spectra of ZnMgFe LDH and ZnMgFe LDH/CTX, and TGA–DTG thermal analysis of (c) ZnMgFe LDH, (d) ZnMgFe LDH/CTX, (e) and (f) scanning electron microscopy images of ZnMgFe LDH/CTX.

have a larger surface area and a greater number of active sites for enhancing the adsorption mechanism.[33]

Fourier transform infrared spectroscopy was performed to understand the formation of chemical bonds resulting during preparation. FTIR spectra of ZnMgFe LDH and ZnMgFe LDH/ CTX nanocomposites were provided in Fig. 3b. As observed for Zn–Fe–Mg LDH, the broad bands that appeared at 3418 cm^{-1} and 1635 cm^{-1} are attributed to the stretching vibrations of hydroxyl groups (–OH), which originated from water molecules and the deformation of metal oxides. Additionally, the band that occurred at 1380 cm^{-1} can be attributed to the bending of nitrate groups arising from metal nitrate salt. All bands below 850 cm^{-1} were assigned to the vibration of the metal–oxygen lattice, M–O, M–OH, and M–O–M vibrations. for ZnMgFe LDH/CTX, the main absorption band at 3418 cm^{-1} in ZnMgFe LDH has shifted to a higher wavelength of 3480 cm^{-1} indicating promoted hydrogen bonding between ZnMgFe LDH

and CTX.[34,35] The intensity of the peak at 1380 cm^{-1} was decreased indicating the exchange of nitrate anions by the CTX.[34] These shifts can be attributed to the contribution of metal ions with oxygen atoms of the drug. Based on frequencies of the FTIR spectra of ZnMgFe LDH and ceftriaxone, the strong band appeared around 1739 cm^{-1} due to carboxylic (C=O) in the ceftriaxone drug. The band at 1604 cm^{-1}, was assigned to (C=N) groups stretching.[36] The broad band at 1100 cm^{-1} is due to aromatic (C–H) bending and (M–O) stretching (overlapped).[36]

The thermal stability and phase transition of the ZnMgFe LDH and ZnMgFe LDH/CTX material were investigated utilizing the TGA/DTG technique. Fig. 3c depicts the TGA/DTG curves of ZnMgFe LDH, which indicated three major weight loss steps. Below 125 °C, the weight loss is ascribed to water removal from the surface and interlayers of the LDH.[36] The second stage, which has a temperature ranging between 125–210 °C, was caused by the dehydration of LDH brucite-like layers. The final

stage (125–650 °C) was attributed to the deformation of the brucite-like layers. The total weight loss that occurred at 880 °C was 41.20%. The mentioned results are consistent with the DTG curve illustrated in Fig. 3c. The DTG curve had three distinct peaks at 125 °C, 210 °C, 650 °C, and 880 °C. The peak at 125 °C was associated with water elimination, the peak at 210 °C with LDH interlayer dehydration, and the peak at 880 °C with recrystallization and nitrate desorption.[37] As shown in Fig. 3d illustrating the TGA/DTA curves for ZnMgFe LDH/CTX, both successive endothermic peaks located at 162 °C and 270 °C were attributed to interlayered water and dihydroxylation removal. There were further mass losses around 640 °C and 819 °C in the TGA/DTA curves, which were caused by the organic guest combustion of ceftriaxone. At 162 °C, the decomposition started, suggesting it was the interaction of ceftriaxone with ZnMgFe LDH through hydrogen bonding, electrostatic attraction, and van der Waals force. This explains how the ZnMgFe LDH/CTX nanostructure was enhanced in thermal stability.

The scanning electron microscopy (SEM) image for ZnMgFe/ LDH after adsorption is shown in Fig. 3e and f and demonstrates a uniformly rough surface with several pores. Aggregates of nanoparticles with a plate-like shape forming flower-like structure Fig. 3e. This change has a great effect on obtaining a high current density, which plays the most important role in its electrocatalytic activity by enabling the easier entrance of reactive species to the active sites.[13]

3.2 ZnMgFe MMO adsorption study

3.2.1 Effect of pH and adsorbent dosage. The effect of pH on CTX adsorption is shown in Fig. 4a. CTX has 3 dissociation constants at $pK_1 = 3$, $pK_2 = 3.2$, and $pK_3 = 4.1$,[38] therefore increasing pH above pK_a leads to negative charge formation on CTX.[39] At low pH values, CTX is positively charged and ZnMgFe LDH has a zeta potential of 35 mV (Fig. 4b). The electrostatic repulsion between both CTX and ZnMgFe LDH is the main reason for the low RE% at pH = 3. In the pH range 5–7, the charge of ZnMgFe LDH is positive (as shown in Fig. 4b) and CTX becomes negatively charged. Therefore, the electrostatic attraction plays a significant role in increasing the observable RE%. In addition, the agglomeration of ZnMgFe LDH is of minimum value as represented by the hydrodynamic size values (Fig. 4c). At higher pH values, electrostatic attraction is outweighed by the high agglomeration of ZnMgFe LDH (Fig. 4c) and RE% decreases. Since ZnMgFe LDH has minimum agglomeration at pH = 5 and RE% was insignificantly different in the range pH = 5–7, the value of pH = 5 was chosen as the optimum pH for further investigations.

Fig. 4b reflects the decrease in the value of the zeta potential of ZnMgFe LDH with a pH increase. This is a common trend for LDH samples where the positive charge of LDH layers decreases with the increase in pH.[40–42] This can be attributed to the deprotonation reaction of LDH with increasing OH⁻ ions
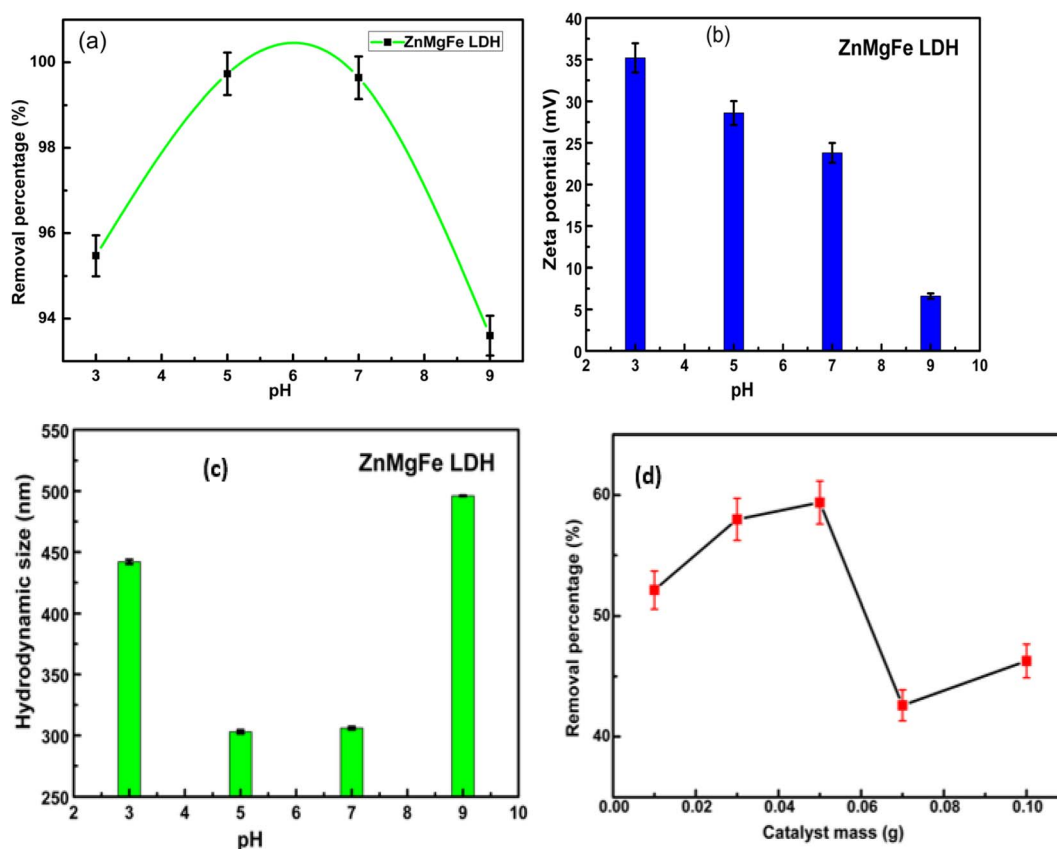

Fig. 4 The effect of (a) pH on the RE% of CTX on ZnMgFe LDH, (b) zeta potential of ZnMgFe LDH at different pH values, (c) hydrodynamic size of ZnMgFe LDH at different pH values, and (d) effect of adsorbent mass on the RE% of CTX on ZnMgFe LDH.

concentration. This reaction can be represented by the following equation for the ZnMgFe LDH sample[43,44]

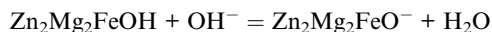$$Zn_2Mg_2FeOH + OH^- = Zn_2Mg_2FeO^- + H_2O$$

Fig. 4d illustrates the effect of the adsorbent dose on the removal efficiency of CTX. The removal efficiency of CTX increased to 59% with a dose of 0.05 g. This may be attributed to the presence of more accessible active sites for adsorption in the ZnMgFe LDH structure. However, the % RE of CTX was reduced upon a further increase in LDH dose. This can be attributed to the aggregation of LDH particles with higher doses.[45] Fig. 4c illustrates the hydrodynamic size of ZnMgFe LDH at different pH values. As shown, when pH values are very low (acidic) or very high (alkaline), excessive agglomeration occurs. This may be attributed to the presence of a high concentration of background ions, originating from the added acid or alkali to adjust the pH value, leading to such agglomeration.

3.2.2 Effect of initial concentration. Various isotherm models (Fig. 5) were investigated to fit the experimental data of ZnMgFe LDH as an adsorbent. The models used were Langmuir,[46] Freundlich,[47] Temkin, Dubinin–Radushkevich (D–R),[48] Langmuir–Freundlich, Sips,[49] Redlich–Peterson,[50,51] Toth,[52] Fritz–Schlunder, and Baudu[53] isotherms. The results show that the Dubinin–Radushkevich model is the most adequate with the highest R^2 value of 0.98 as illustrated in Table 2. Using higher parameter isotherms did not correspond to improving the value of R^2. Other statistical error functions were computed, and the results are illustrated in Table 3. D–R isotherm is

a generalized model compared to the classical Langmuir model. D–R model does not include an assumption for the presence of a homogenous surface or constant adsorption potential throughout its derivation.[54] D–R model reflects that CTX adsorption on the ZnMgFe LDH is a physical adsorption process in nature with multilayer formation.[55]

3.2.3 Adsorption kinetics. Fig. 5d shows the adsorption kinetics of CTX where equilibrium was reached below 10 minutes. All models showed a high value of R^2 of 0.99 (Table 4). Other statistical error functions were computed, and the results are illustrated in Table 5. The mixed first and second order showed the least error. This is considered the most suitable model for the kinetics data. This equation is an advanced form of adsorption kinetics modeling compared to both the first and second orders.[57] It is considered a combination of both the first and second-order equations in one generic model suitable for real-life adsorption studies.[57]

3.2.4 Effect of temperature. The effect of adsorption temperature was investigated at the optimum conditions at various temperatures: 25–55 °C. Fig. 5e shows the decrease in removal efficiency of CTX with increasing the temperature of adsorption. This indicates the exothermic nature of the adsorption process where adsorption decreases with temperature according to Le Chatelier's principle.[58] Values of $\Delta G°$, $\Delta S°$, and $\Delta H°$ are shown in Table 6. Fig. 5f shows an inverse relationship between the absolute temperature and ln K_d where $\Delta S°$ was calculated from the intercept and the slope of the straight-line (adjusted $R^2 = 0.9$). Such inverse relation reflects the weakness of bonding between CTX and the synthesized ZnMgFe LDH adsorbent.[59,60]
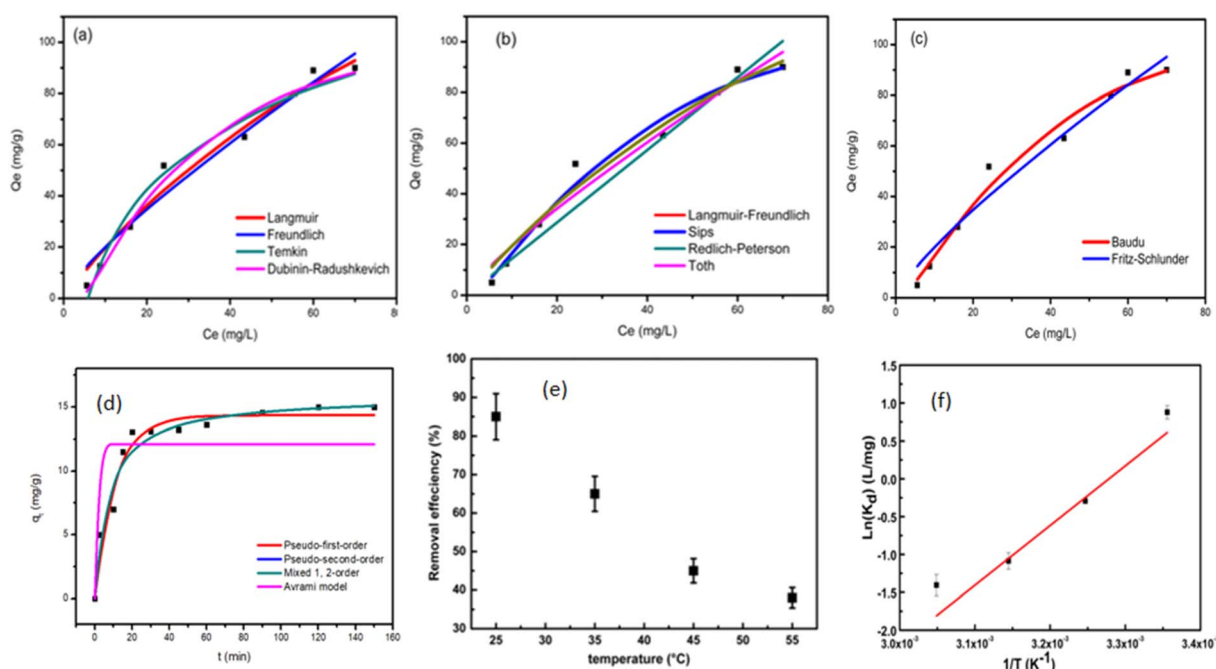

Fig. 5 Isotherm plots for CTX adsorption onto ZnMgFe LDH (a) two parameter isotherm models (b) three-parameter isotherm models, (c) higher parameter isotherm models (d) kinetic modeling of CTX adsorption on ZnMgFe LDH, and plot of (e) removal efficiency *vs.* temperature and (f) ln(K_d) *versus* inverted temperature, $1/T$ (K^{-1}).

Table 2 The non-linear adsorption isotherm models using ZnCoFe MMO as adsorbent

Isotherm models	Equation	Model parameters		Values	R^2
Two-parameters isotherm					
Langmuir	$q_e = \dfrac{q_{max}K_L C_e}{1 + K_L C_e}$	q_{max} (mg g^{-1})	A parameter that reflects monolayer formation	241.75	0.97
		K_L (L mg^{-1})	Adsorption equilibrium constant	0.0089	
Freundlich	$q_e = K_f C_e^{1/n_f}$	K_f (L g^{-1})	A constant for the relative adsorption capacity	3.13	0.96
		$1/n_f$ (—)	Constant indicative of surface heterogeneity	0.8	
Temkin	$q_e = (RT/b_T)\ln(A_T C_e)$, R is the universal gas constant and T is the absolute temperature	b_T	Temkin isotherm constant	70.73	0.97
		A_T (L g^{-1})	Isotherm equilibrium binding constant	0.17	
Dubinin–Radushkevich	$q_e = (q_m)\exp(-K_{ad}\varepsilon^2)$; $\varepsilon = RT(1 + (1/C_e))$	q_m (mg g^{-1})	Theoretical adsorption capacity	122.42	0.98
		K_{ad} (mol^2 kJ^{-2})	Constant related to adsorption energy	0.0046	
Three-parameters isotherm					
Langmuir–Freundlich		q_{max} (mg g^{-1})	Max. adsorption capacity	119.02	0.98
		K_{LF} (L mg^{-1})	Equilibrium constant	0.029	
		β_{LF} (—)	Heterogeneity parameter	1.52	
Sips	$q_e = \dfrac{q_{max}K_S (C_e)^{n_s}}{1 + K_S (C_e)^{n_s}}$	q_{max} (mg g^{-1})	Sips maximum adsorption capacity	119.04	0.98
		K_s (L mg^{-1})	Equilibrium constant	0.0047	
		n_s (—)	Sips' model exponent	1.52	
Redlich–Peterson	$q_e = \dfrac{q_{max} C_e}{1 + K_S (C_e)^{\beta_s}}$	q_{max} (L mg^{-1})	Isotherm constant	1.43	0.94
		K_s (mg g^{-1})	Isotherm constant	0	
		β_s (—)	Isotherm constant	0	
Khan	$q_e = \dfrac{Q_m b_K C_e}{[1 + (b_K C_e)]^{a_K}}$	Q_m	Isotherm constant	2942.86	0.97
		b_K	Isotherm constant	0.0007	
		a_K	Isotherm constant	9.4	
Toth	$q_e = \dfrac{K_e C_e}{[1 + (K_L C_e)^n]^{1/n}}$	K_e (mol L mg^{-1} mg^{-1})	Tóth max. adsorption capacity	2.60	0.96
		K_L (L mg^{-1})	Tóth equilibrium constant	3.51	
		n (—)	Tóth model exponent	0.20	
Higher-parameters isotherm					
Baudu	$q_e = \dfrac{q_{max} b_o (C_e)^{1+x+y}}{1 + b_o (C_e)^{1+x}}$	q_{max} (mg g^{-1})	Baudu max. adsorption capacity	119.10	0.98
		b_o (—)	Equilibrium constant	0.0047	
		X (—)	Baudu parameter	0	
		Y (—)	Baudu parameter	0.519	
Fritz–Schlunder	$q_e = \dfrac{q_{mFSS}K_1 (C_e)^{m_1}}{1 + K_2 (C_e)^{m_2}}$	q_{mFSS}	Fritz–Schlunder maximum adsorption capacity (mg g^{-1})	17.22	0.96
		K_1	Model parameter	0.27	
		K_2	Model parameter	0.49	
		m_1	Model parameter	0.83	
		m_2	Model parameter	0.08	

Table 3 Statistical error functions calculated for the isotherm models[56]

	Root mean square error (RMSE)	Normalized root mean square error (NRMSE)	Mean absolute error (MAE)	Mean bias error (MBE)	Mean absolute percentage error (MAPE) (%)
Langmuir	5.068	0.097	4.36	0.872	26.3
Freundlich	5.833	0.111	4.799	0.668	29.4
Temkin	5.261	0.1	4.4	0	24.9
Dubinin–Radushkevich	4.373	0.083	3.573	−0.397	13.1
Langmuir–Freundlich	4.272	0.082	3.261	0.244	11.7
Sips	4.272	0.082	3.262	0.243	11.7
Redlich–Peterson	7.494	0.143	4.986	−1.65	16
Khan	4.981	0.095	4.266	0.802	25.2
Toth	5.823	0.111	4.639	0.414	27.3
Baudu	4.272	0.082	3.264	0.243	11.7
Fritz–Schlunder	5.827	0.111	4.811	0.532	29.5

Table 4 Kinetic study model fitting parameters

Kinetic model	Kinetic equation	Model parameters	Values
Pseudo first order	$q_t = q_e(1 - e^{-K_1 t})$, q_e is the adsorption capacity at equilibrium, k_1 is the pseudo-first-order rate constant	K_1 (min^{-1}) q_e (mg g^{-1}) R^2	0.094 14.36 0.92
Pseudo second order	$q_t = \dfrac{q_e^2 K_2 t}{1 + q_e K_2 t}$, k_2 is the pseudo-second-order rate constant	K_2 (g (mg^{-1} min^{-1})) q_e (mg g^{-1}) R^2	0.0086 15.82 0.93
Mixed first and second order	$q_t = q_e \dfrac{1 - e^{-Kt}}{1 - f_2 e^{-Kt}}$, f_2 is the mixed 1st, 2nd order coefficient, k is the adsorption rate constant	K (min^{-1}) q_e (mg g^{-1}) f_2 (g (mg^{-1} min^{-1})) R^2	0.00022 15.8 0.99 0.93
Avrami model	$q_t = q_e(1 - [e^{-K_{av}t}]^{n_{av}})$, k_{av} is the Avrami rate constant and n_{av} is the model's component	K_{av} (min^{-1}) n_{av} (—) q_e (mg g^{-1}) R^2	3 5.47 12.1 0.56

Table 5 Statistical error functions calculated for the kinetic models

Model	RMSE	NRMSE	MAE	MBE	MAPE (%)
Pseudo first order	0.894	0.081	0.75	−0.06	9.2
Pseudo second order	0.863	0.078	0.58	−0.001	6.8
Mixed first and second order	0.863	0.078	0.58	−0.001	6.8
Avrami model	3.09	0.281	2.328	0.001	31

Table 6 Thermodynamic parameters for CTX adsorption process onto MMO

Material	T (K)	$\Delta G°$ (kJ mol^{-1})	$\Delta H°$ (kJ mol^{-1})	$\Delta S°$ (J mol^{-1} K^{-1})
ZnMgFe LDH	298	−2.174	62.54	−204.051
	308	0.747		
	318	2.874		
	328	3.835		

3.2.5 Possible adsorption mechanism. ZnMgFe LDH consists of a layered structure built from the octahedrons of Zn, Mg, and Fe centers surrounded by OH groups as shown in Scheme 2. CTX and ZnMgFe LDH can interact in different mechanisms as illustrated in Scheme 2. One possible mechanism is the interaction between positive cations (Zn, Mg, and Fe) in the octahedral position of the LDH layer and CTX atoms having lone electron pairs. Another interaction mechanism is the hydrogen bonding possibly formed between hydrogen and oxygen on the surface of the LDH layers.[61] After the monolayer formation of CTX molecules, multilayers may form as indicated by the suitability of D–R model for isotherm data.

As illustrated in Table 7, which compares the results of the prepared material to other adsorbents, ZnMgFe showed 99.7% removal efficiency for CTX. To estimate the significance of the prepared material for wastewater remediation from CTX, the maximum adsorption capacity estimated was compared to other adsorbents. This study opens new routes for recycling waste adsorbents after adsorption. Such reused materials can be further utilized as electro-catalysts showing promising performance and multi-functionality as antimicrobial agents as well.

3.3 Methanol electro-oxidation using the spent ZnMgFe LDH

The electrochemical performance of both ZnMgFe LDH and ZnMgFe LDH/CTX was assessed using cyclic voltammetry between 0.0 and 0.6 V (*vs.* Ag/AgCl) at scan rates of 5, 10, 20, 30, 40, 50 and 60 mV s^{-1}. As shown in Fig. 6a and b, the spent ZnMgFe LDH/CTX shows around a 10-fold increase in electrochemical activity for all scan rates investigated.

The maximum current density recorded at each methanol concentration is summarized in Table 8. As methanol concentration increases, the maximum current density generated by both the ZnMgFe LDH and ZnMgFe LDH/CTX samples increases. At a methanol concentration of 0.5 M, the current of the ZnMgFe LDH/CTX sample (after adsorption) was 8 folds that of the ZnMgFe LDH sample (before adsorption) (Fig. 6c). The maximum recorded value of current density for ZnMgFe LDH/CTX was 47 mA cm^{-2} at a methanol concentration of 3 M (Fig. 6d). The value of folds after adsorption decreased with increasing methanol concentration reaching 4.7 folds at 3 M methanol.

Fig. 6e displays the relationship between the anodic peak current density *versus* the square root of the scan rates for ZnMgFe LDH and ZnMgFe LDH/CTX. As shown, the liner relationship reflects that the electro-catalytic oxidation of methanol
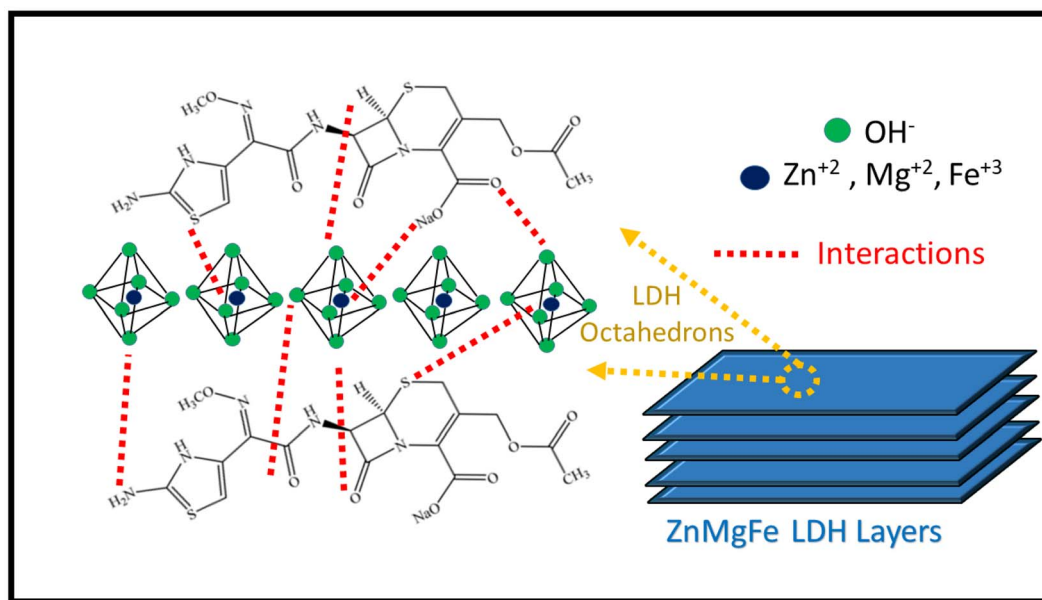
Scheme 2 Possible adsorption mechanisms of CTX on ZnMgFe LDH nano-adsorbent.

Table 7 Recent studies reporting the adsorption of CTX compared to the current study

Adsorbent	pH	CTX conc. (mg L^{-1})	Equilibrium time (min)	Adsorbent mass (g)	Removal percent (%)	Q_{max} (mg g^{-1})	References
ZnMgFe LDH	5	50	10	0.05	99.7	241.75	This work
ZnCoFe mixed metal oxide	7	50	60	0.05	85	322	62
TiO$_2$/chitosan/nano-bentonite	5	25	10	2	93.5	90.9	63
Pseudomonas putida biomass	7	50	120	0.1	50	109.5	64
C$_3$N$_4$/MWCNT/Bi$_2$WO$_6$	4	50	10	0.015	98.4	19.6	65
Fe$_3$O$_4$/activated carbon	3	10	90	1.99	97.1	28.9	66

over both samples is a diffusion-controlled process.[14] It is necessary to consider the stability of electro-active electrode materials, which can be assessed through various tests such as chronoamperometric (CA) measurements. CA of both ZnMgFe LDH and ZnMgFe LDH/CTX is presented in Fig. 6f. As shown, both samples possess reasonable stability over a 3600 S time window with no significant deterioration of electrochemical performance. Therefore, the spent ZnMgFe LDH/CTX can be considered a stable electro-oxidation catalyst for methanol fuel cell applications.

Table 9 illustrates the different values of current density for methanol electro-oxidation reported by different studies. As shown, spent ZnMgFe LDH/CTX exhibited the highest value compared to spend adsorbents. Moreover, this spent adsorbent showed higher current density values than some fresh LDH catalysts reported in the literature.

3.4 Measurements of total organic carbon (TOC)

To check the effect of cyclic electrooxidation of methanol on the surface of spent ZnMgFe LDH/CTX, the measurements of total organic carbon (TOC) were checked. For this issue, samples of the electrolyte were drawn from the electrolytic cell for TOC analysis during repeated cycles for methanol oxidation at 1 M KOH, and 3 M of methanol at 50 mV s^{-1} scan rate. The selected cycles of methanol oxidation were (1, 10, 20, 30, and 40 cycles).

As shown in Fig. 7, the noticeable decrease in TOC concentration was caused by methanol oxidation on the spent ZnMgFe LDH/CTX, this behavior could be assumed to the oxidative transformation of methanol into the inorganic carbon represented by CO$_2$ and carbonates. Based on these results, the methanol concentration in KOH as the electrolyte is reduced to 25% after 40 cycles owing to the electrochemical activity of the spent ZnMgFe LDH/CTX electrode which confirms its oxidation into inorganic carbon.[72]

The possible mechanism of methanol electro-oxidation over ZnMgFe LDH/CTX is illustrated in Scheme 3. The role of LDH electro-catalysts in methanol oxidation is still not fully understood. The metallic centers are thought to form oxyhydroxides leading to methanol oxidation, which is known as the Fleishmann mechanism.[73] The synergy between different metallic centers is also an important factor that should be considered for layered double hydroxide catalysts.[74] The adsorption of CTX adds complexity to the interpretation of the methanol electro-oxidation mechanism. It was reported that polymer binders
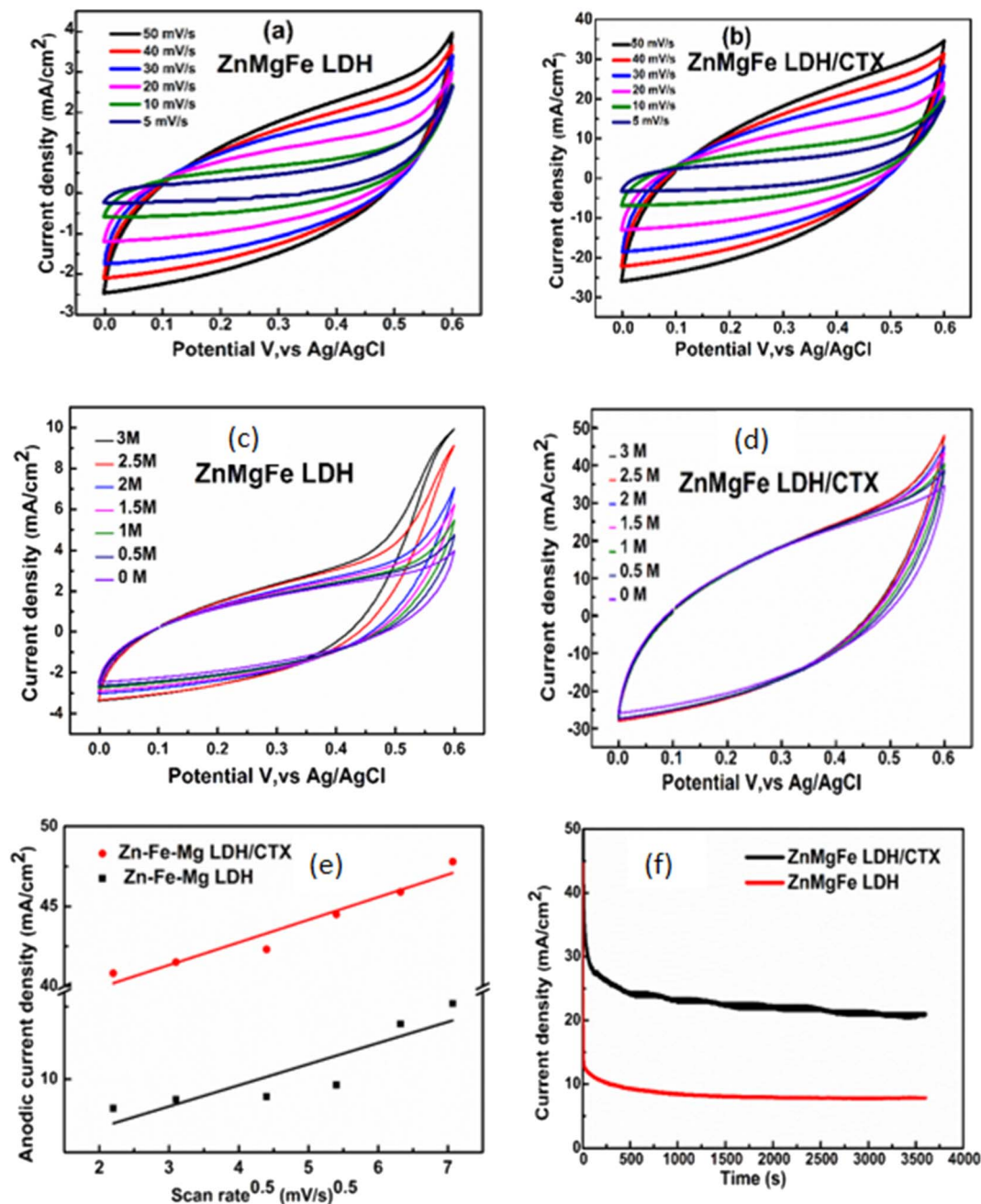
Fig. 6 Cyclic voltammograms of (a) ZnMgFe LDH and (b) ZnMgFe LDH/CTX in 1 M KOH at different scan rates in a potential window of 0.0−0.6 V (*vs.* Ag/AgCl), (c) ZnMgFe LDH and (d) ZnMgFe LDH/CTX in 1 M KOH at different methanol concentrations in a potential window of 0.0−0.6 V (*vs.* Ag/AgCl), (e) the relationship between the current density peaks and the square root of the scan rates for ZnMgFe LDH and ZnMgFe LDH/CTX, and (f) chronoamperometric stability curves for ZnMgFe LDH and ZnMgFe LDH/CTX (3 M methanol) solution at room temperature at 0.6 V (*vs.* Ag/AgCl) in 1 M KOH.

may negatively affect the current density of methanol electro-oxidation.[74] This was not the case since all results by the spent adsorbent showed better results compared to the fresh LDH adsorbent. In this study, CTX can be regarded as a coordination compound or a ligand attached to the layered structure of ZnMgFe LDH. Coordination molecules were reported to have a positive contribution to the value of current density for metallic catalysts.[75] Most studies of coordination compounds contain metal centers and the mechanism of their action is still debatable. In this study, the role of CTX is assumed to interact with the octahedrons forming the layered structure of LDH. This interaction enhances the valence of the metallic centers thereby increasing their potential towards oxidizing the methanol molecule. However, more studies are required to understand the role of CTX and/or similar molecules on the oxidation of methanol and similar small organic molecules.

Table 8 Values of the maximum current densities at different methanol concentrations ZnMgFe LDH and ZnMgFe LDH/CTX

Methanol concentration (M)	Current density of ZnMgFe LDH (mA cm^{-2})	Current density of ZnMgFe LDH/CTX (mA cm^{-2})	Folds increase after adsorption
0.5	4.5	36	8.00
1.0	5.4	37	6.85
1.5	6.0	40	6.66
2.0	7.0	41	5.85
2.5	9.0	43	4.77
3.0	10.0	47	4.70

Table 9 Comparison of methanol electro-oxidation activity reported in this work with reported LDH studies

Material	Methanol concentration (M)	Scan rate (mV S^{-1})	Current density (mA cm^{-2})	References
Spent ZnMgFe LDH/CTX	**3**	**50**	**47.00**	**This work**
Spent CoNiZnFe LDH after methyl orange adsorption	1	50	6.66	14
Spent CoNiZnFe LDH after methyl orange adsorption calcined at 200 °C	3	50	8.40	14
Spent ZnCoFe LDH after methylene blue adsorption	3	50	12.61	67
Spent ZnCoFe LDH after oxytetracycline adsorption	1	50	20.00	15
ZnMgFe LDH	**3**	**50**	**10.00**	**This work**
NiFe-LDH carbon xerogel supported on nickel foam	0.5	10	400.00	68
NiCo-LDH nanowires on a nickel foam	0.5	10	761.00	69
3D NiCr-LDH/reduced graphene oxide	3	—	2.22	70
Ni–Cr LDH	3	60	7.02	71

3.5 Antimicrobial study of ZnMgFe LDH

3.5.1 Anti-bacterial assay. These investigations are limited by the lack of animal debridement, the high initial inoculum, and the lack of experience with recurrent or chronic infection. Experimental models also prevent long-term follow-up. Various dangerous pathogens were used to study anti-Gram-positive medicines, representing many but not all patient infections. Fig. 8a and b show the ZnMgFe LDH's MIC and MBC against the bacterial species. The findings show that ZnMgFe LDH MIC values vary greatly across species. Most microorganisms have equal MBC and MIC values, suggesting bactericidal action.

Fig. 7 Total organic carbon with repeated cycles over spent ZnMgFe LDH/CTX at 1 M KOH, 3 M of methanol, and 50 mV s^{-1} scan rate.

Listeria monocytogenes and *Haemophilus influenza* had MIC values of 228 µg mL^{-1}, whereas *Staphylococcus aureus* and *S. Pyogenes* had MIC values of 4.6 and 6.6 µg mL^{-1}, respectively. *B. subtilis* and *E. coli* had 12.8 and 20 µg mL^{-1}. ZnMgFe LDH killed MBC in Fig. 8b.

Fig. 8c depicts agar plates containing many bacterial strains, including Gram-positive *S. pneumonia* (ATCC 49619), *S. aureus* (ATCC 25913), *Listeria monocytogenes* (ATCC 19115), and Gram-negative *E. coli* (ATCC 25922) and *Haemophilus influenza* (ATCC 49766) and *Bacillus subtlis* (ATCC 35021). Moreover, Fig. 9 depicts the inhibition zone of each strain at various ZnMgFe LDH concentrations. Using the agar diffusion method, the inhibition zone was calculated in millimeters. The measured sizes of several species were distinct overall. As a result, Fig. 8c is a bar graph displaying the calculated mean of the inhibitory zone (mm) at different doses of ZnMgFe LDH (1000, 500, 250, 125 µg mL^{-1}) *vs.* the diverse kinds of bacteria mentioned before along the *X*-axis. In general, the effect of ZnMgFe LDH on the tested strains was inconclusive. Regarding Gram-positive bacteria, *S. Pyogens*, *Staphylococcus*, and *Bacillus subtilis* had the greatest reaction rates (30 & 29 mm) whereas Gram-negative bacteria had the lowest response rates. *H. influenza* and *E. coli*. In addition, Fig. 8c shows that the inhibition zone was proportional to the ZnMgFe LDH concentration in all examined species. *S. Pyogens*, a Gram-positive bacterium, has the greatest inhibitory zone, extending around 30 millimeters, while *E. coli* displayed the smallest, measuring approximately 24 millimeters. Notably, the tested ZnMgFe LDH was compared to doxycycline for both Gram-negative and Gram-positive organisms (24 mm), and the results revealed that the effect of ZnMgFe LDH and the compared standard drug was hardly the same in both
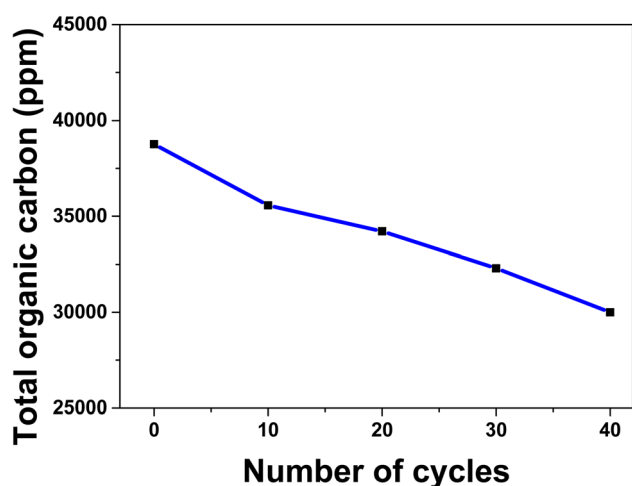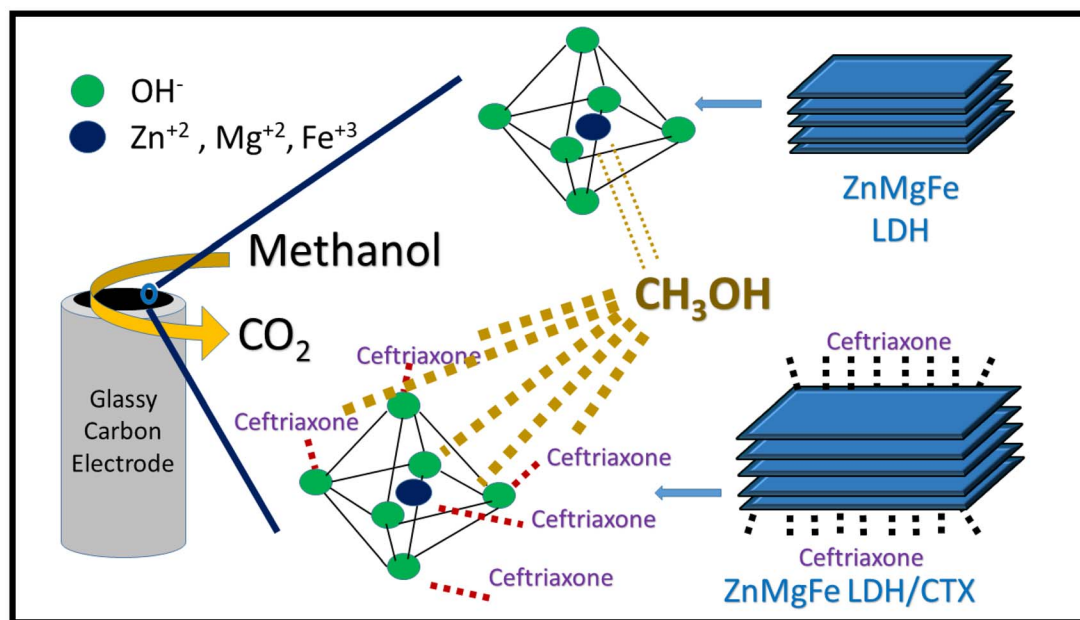
Scheme 3 Possible mechanism of methanol electro-oxidation enhancement using ZnMgFe LDH/CTX.

Gram-negative and positive organisms, with ZnMgFe LDH being more effective against spore-forming bacteria such as *Bacillus subtilis*. From this viewpoint, the studied ZnMgFe LDH might serve as a viable alternative to conventional antibiotics in reducing bacterial resistance.

Regarding the fungal broth microdilution test for ZnMgFe LDH, a lot of studies have investigated the interaction of nanomaterials with bacteria, but only a few have investigated their effect on fungi. This might be due to the relative simplicity of bacterial and fungal systems.[76] According to this study's antifungal inquiry, ZnMgFe LDH severely impacts *Mucor* strain. *Mucor* contagious species, like other invasive fungal illnesses, cause immunosuppression (especially delayed and excessive neutropenia, a severe hematological disease with or without stem cell transplantation, and delayed corticosteroids) that predisposes to *Mucormycosis*.[77] Iron overload, poorly managed diabetes mellitus with or without diabetic ketoacidosis, and deferoxamine-containing medications increase risk.[78] Aspiratory or rhino-orbito-cerebral fungal spores are the main cause of *Mucormycosis*. After burns, *Mucorales* spp. infections have grown.[79] Infections may occur without risk factors. Insect bites and animal scrapes sometimes allowed spores to enter tissue.[80] *Mucormycosis* of the gastrointestinal system, especially from ingested spores, has also been documented.[81] All *Mucormycosis* invade blood arteries and cause thrombosis and tissue damage. Angio-invasion also explains *Mucormycosis* infection spread.[82] *Mucormycosis* is distinguished from conspicuous *Aspergillosis* by its histological abnormalities, quick dynamic character, and extensive tissue rot. Diabetes, press overload, and deferoxamine medication increase *Mucormycosis* risk. This fungus is dangerous, thus new antifungal medications to treat or prevent severe fungal infections are needed.

As demonstrated in Fig. 8d and e, the MICs for all of the tested isolates were similar to the MFCs, indicating the fungicidal activity of ZnMgFe LDH. The ZnMgFe LDH was effective against all fungi, especially *Mucor*, *Aspergillus* species, and *Penicillium* strains (166 and 83 μg mL^{-1}, respectively). They displayed antifungal activity against other species, including *A. flavus* (250 μg mL^{-1}), at greater concentrations. As seen in Fig. 8e, the MFC for ZnMgFe LDH demonstrated outstanding fungicidal activity against *Penicillium* and *Mucor* (83 and 166 μg mL^{-1}, respectively).

An experiment with sorbitol was repeated and analyzed to assess the nanomaterial's antifungal activity (ZnMgFe LDH's antifungal mechanism). To determine the specific method of action of the examined drugs against varied fungal strains, the MIC values were repeated on various sorbitol mediums. A lower effective MIC indicates an impact on the fungal cell wall. Despite higher MIC values, ZnMgFe LDH was more potent against *Penicillium*, *Mucor*, and *A. fumigatus* at 62 and 85 μg mL^{-1}. Fig. 9. Sorbitol stabilizes fungal protoplasts osmotically. Some cell wall inhibitors of fungi are neutralized by sorbitol.[83] Cells protected by sorbitol may proliferate in the presence of fungal cell wall inhibitors, but proliferation would be inhibited in the absence of sorbitol. The drop in MIC value recorded in media containing sorbitol compared to media without sorbitol demonstrates this effect (standard medium).[84] Osmotic destabilizing agents and cell wall disruption result in the rearrangement of the cell wall, enabling fungal cells to survive.[85]

In addition to restricting spore germination, proliferation, and cellular respiration, the chemicals investigated seemed to affect the cell wall by modifying its structure, decreasing its production, and triggering cell death. In addition to reduced effective fungicidal concentrations against *Mucor* and *Penicillium*, the MFC results using a different medium with extra
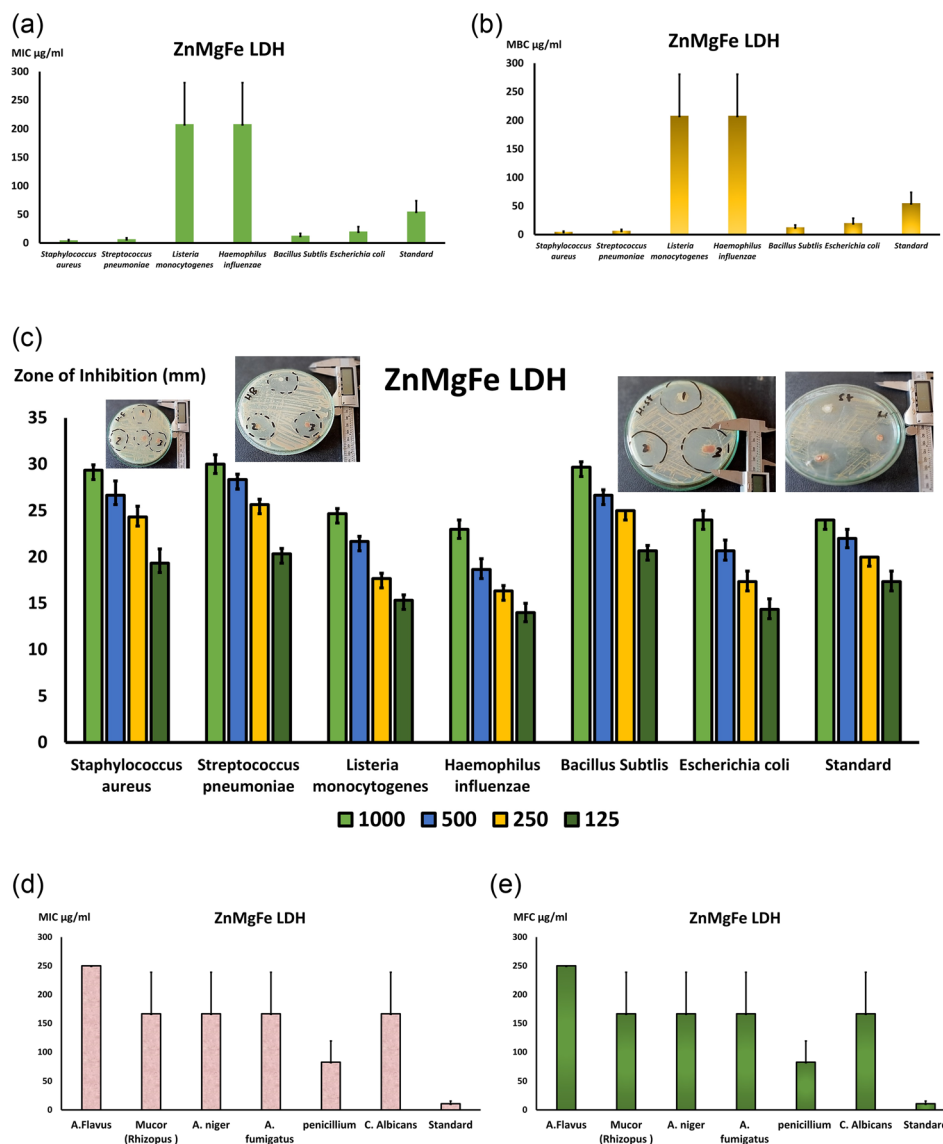
Fig. 8 (a) Presents the MIC values and (b) the MBC values of ZnMgFe LDH against both Gram-positive bacteria, and Gram-negative bacterial (mean ± SE), (c) illustrates the calculated mean of the inhibition zone (mm) at different concentrations of ZnMgFe LDH *versus* diverse species of bacteria, and the mean of inhibition zone against standard antibiotics (doxycycline for both Gram-negative and Gram-positive), (d) presents the MIC values (μg mL^{-1}) and (e) the MFC values (μg mL^{-1}) of ZnMgFe LDH against both different fungal isolates (mean ± SE).

sorbitol concentrations demonstrated lower fungicidal concentrations against the same species. As demonstrated in Fig. 9a and b, the MFC concentration for *Penicillium* and *Mucor* fell to 62 and 85 μg mL^{-1}, respectively.

The disc diffusion technique is recognized as one of the most accurate methods for assessing antifungal or antibacterial activity. On SDA plates, inhibitory zones against a variety of fungal strains were evaluated, and Fig. 9c depicts a variety of concentrations. ZnMgFe LDH displayed a good zone of inhibition against *Aspergillus*, *Penicillium*, and *Candida* at 1000, 500, and 250 μg mL^{-1}, in contrast to the traditional antifungal for quickly growing fungi (chlorohexidine). According to Fig. 9c, ZnMgFe LDH showed good antifungal efficacy against the other fungal strains.

Relating to antifungal activity (inhibition percentage), the percentage of fungal inhibition was computed based on the assessment of antifungal activity after the addition of materials to the medium and is shown in Fig. 9d. ZnMgFe LDH inhibited *Mucor* at a rate of 73%, whereas *Candida* was inhibited at a rate of 71%. The antifungal activity of ZnMgFe LDH is a consequence of its unique characteristics, such as its small size, large surface area, and uniform dispersion. Eighty percent is the greatest inhibitory percentage against *A. fumigatus* isolates.

Antimicrobial resistance is responsible for significant social and economic losses. The World Health Organization estimates that antibiotic resistance causes 700 000 annual deaths worldwide. By partially releasing metallic ions in aqueous dispersion, the usage of layered double hydroxides (LDHs) as antibacterial
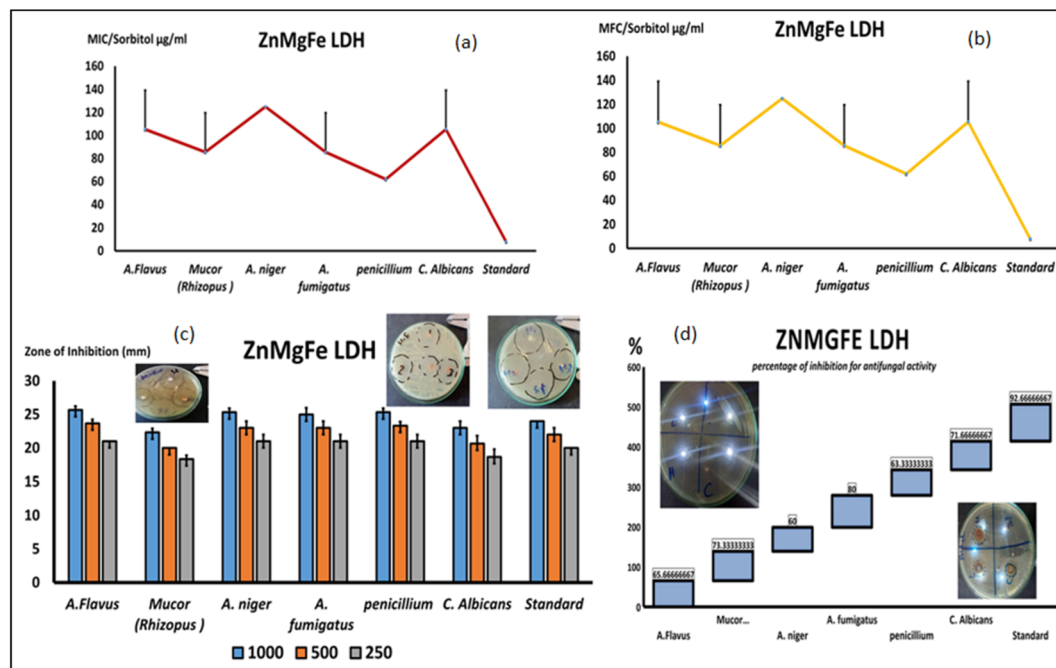
Fig. 9 (a) Presents the MIC values ($\mu g\ mL^{-1}$) and (b) the MFC values ($\mu g\ mL^{-1}$) of ZnMgFe LDH on sorbitol media against both different fungal isolates (mean $\pm$ SE), (c) illustrates the calculated mean of the inhibition zone (mm) at different concentrations of ZnMgFe LDH *versus* diverse species of fungi, and the mean of inhibition zone against standard antibiotics (cycloheximide) (mean $\pm$ SE), (d) percent of inhibition (%) of ZnMgFe LDH in SDA media against multiple fungal strains.

materials might provide a means to lower the risk of bacterial infections and antibacterial resistance. In the growth medium of *Escherichia coli* (*E. coli*) and *Staphylococcus aureus* (*S. aureus*), the partial dissolution of various synthetic LDHs M(II)–Al(III) (M = Zn, Cu, Ni, Co, Mg) was investigated. Several characteristics (crystallinity, M(II) : Al(III) ratio, type of intercalated anion, and nature of M(II) cations) were studied to determine their effect. LDHs which is composed of Zn(II) and Cu(II) exhibited antibacterial action. The antibacterial action of the investigated LDHs was connected first to the type of the divalent metal and then to the quantity of MII ions released into the culture medium. This impact was recognized more readily in several LDHs whose lowest inhibitory concentration reduced dramatically as greater quantities of connected ions were released from LDH-tested material.[86]

Recent studies on the antibacterial activity of pure LDHs such as MgAl-LDH, MgFe-LDH, and ZnAl-LDH have been very limited.[87–89] In these studies, however, the large doses (316–14,000 $\mu g\ mL^{-1}$) and cumbersome manufacturing techniques (heating >80 °C or >2 h aging period) of LDHs hinder their antibacterial applicability. To prevent these flaws, LDHs might be replaced with antibacterial transition metal ions using a different technique. Due to their effective antibacterial action,[90–93] multiple ions have been frequently used in the manufacture of inorganic antimicrobial drugs. Among the high-valent cations studied, such as Al or Zn, the toxicity of ions to bacteria was the lowest.[94] Thus, Mg, Mn, Cu, Ni, and Co assembled in Al-based LDHs (MAl-LDHs, M: Mg, Mn, Cu, Ni, and Co) with nano production and a good performance against Gram-negative (*Escherichia coli*) and Gram-positive

(*Staphylococcus aureus*) bacteria are urgently required for practical antibacterial application. To our knowledge, little or no prior research has shown the effectiveness of LDH against fungal infections.

Even though, the real process or connection between metal inorganic framework structures and different illnesses has never been defined, several examples are possible. Consistent with the previous study, the inhibitory antibacterial action of ZnMgFe LDH may be related to the production of reactive oxygen species by its components, such as Zn, Mg, Fe, and Al. It is possible that the antibacterial action of ZnMgFe LDH was caused by the spontaneous generation of free radicals such as ROS, therefore triggering oxidative stress-mediated cell damage. Antibacterial activity in MgZnFeLDH might be due to increased reactive oxygen species (ROS).[95] In addition, the shape of nanomaterials may affect their antibacterial activity. The release of metal ions, which may infiltrate into bacterial cells and alter their amino acid metabolism and enzyme system,[96,97] is another potential antibacterial mechanism. Similar to that of bacteria, the antifungal activity of ZnMgFe LDH may be caused by an electrostatic contact between the LDHs and the fungal surface.

In addition, it was shown that ZnMgFe LDH permanently altered membrane features (charge, intra and extracellular permeability, and physicochemical properties). As the mechanism underlying the antibacterial effect of ZnMgFe LDH, changes in cell surface hydrophobicity, charge, enhanced PI absorption, and K^+ leakage with local membrane rupture or hole formation in Gram-negative and positive bacteria were identified. These results are consistent with previous studies on

the specific antibacterial mode of action of ZnMgFe LDH. The antimicrobial activity of LDH is dependent on the interaction between the LDH surface and the bacterial cell wall. The cell walls of both types of bacteria are composed of a layer of lipopolysaccharides linked to lipids by weak covalent bonds. The electrostatic interaction between the positive charges on the LDH surface and the negative charges on the lipopolysaccharides reduces the charge density on the bacterial surface, resulting in a decrease in bacterial cell viability; additionally, the large surface area of LDH contributes to its antimicrobial activity.[98,99] The precise methods by which these nanostructures cause harm to bacterial cells are yet unknown; nevertheless, significant emphasis has been paid to the morphological alterations that occur during *in vitro* investigations using these nanostructures. Three hypothesized processes are most widely acknowledged and documented in the scientific literature: (1) metal ion uptake (translocation and particle internalization) into cells followed by depletion of intracellular ATP production and disruption of DNA replication,[100] (2) generation of ROS (reactive oxygen species) from metal nanoparticles and metal ions, with subsequent oxidative damage to the cellular structures, and (3) accumulation and dissolution of metal nanoparticles within bacterial membranes resulting in changes in their permeability (the progressive release of labile ions).[101]

Hydrophobicity plays a critical role in the attachment of several bacterial species to their substrates, which is an additional element in the antibacterial activity of ZnMgFe LDH.[102] There is substantial interaction between bacteria and hydrophobic surfaces, resulting in high cell attachment rates, according to research.[59] Bacterial adhesion to biotic and abiotic surfaces may be a source of severe infections in hospitals.[103] Therefore, it is important to develop hyper hydrophilic surfaces that decrease bacterial interaction with the substrate. Super hydrophilic surfaces provide a thin layer of water in a physiological environment, which may limit the formation of bacterial biofilms by reducing bacterial adhesion.[104] Ji *et al.*[105] discovered that increasing the hydrophilicity of titanium surfaces reduced the adhesion of *E. coli*. Furthermore, the surface roughness may influence bacterial adherence. Studies indicate that nanoscale roughness has antiadhesive characteristics. Research on both Gram-negative and Gram-positive bacteria revealed this fact. Thus, the surface roughness of LDH may have contributed to their capacity to prevent bacterial adhesion.[106] In this study, ZnMgFe LDH showed the greatest antibacterial activity; few investigations have demonstrated that LDHs have antimicrobial action against Gram-positive and Gram-negative bacteria in addition to their antifungal activity.

4. Conclusions and future prospective

This work focused on investigating ZnMgFe LDH as a 2D adsorbent for the removal of CTX as a model pollutant from wastewater effluents. ZnMgFe LDH was successfully prepared using a facile co-precipitation technique. ZnMgFe LDH was characterized using SEM, XRD, BET, FTIR, and zeta potential

measurements. ZnMgFe LDH was shown to be a promising nano-adsorbent for CTX with a removal efficiency reaching 99%. The spent adsorbent ZnMgFe LDH/CTX was reused as an electro-catalyst for methanol fuel cell applications. The spent adsorbent showed a maximum recorded current density value of 47 mA cm^{-2} at a methanol concentration of 3 M. After adsorption, the current density reached four to eightfold that of the as-prepared adsorbent. This reflects the promising performance of the spent adsorbent for methanol electro-oxidation fuel cell applications. In addition, the antibacterial activity of ZnMgFe LDH against a range of severe illnesses produced by several harmful bacterial and fungal strains was assessed. In light of this, the study suggests that ZnMgFe LDH might replace conventional antibiotics for bacterial or fungal infections in humans and animals. This research paves the way for the commercialization of effective nanomaterial in various applications, such as adsorption and electrocatalysts in methanol oxidation. The successful reutilization of spent adsorbents facilitates the achievement of circular economy principles and large-scale sustainable wastewater adsorption units.

Author contributions

Conceptualization, A. E. A., and R. M.; methodology, H. M., A. A., F. I. A. E.-E., and A. E. A.; software, H. M., and F. I. A. E.-E.; validation, A. F., and R. M.; analysis, R. M., A. F., A. E. A., and A. A.; investigation, A. A., F. I. A. E.-E., and A. F.; resources, R. M., A. F., and A. A.; data curation, H. M. and R. M.; writing—original draft preparation, H. M., R. M., A. E. A., and A. A.; writing—review and editing, all authors; visualization, all authors; supervision, A. E. A., A. F., and A. A.; project administration, A. F., and R. M. All authors have read and agreed to the published version of the manuscript.

Conflicts of interest

The authors declare that they have no competing interests.

References

1 S. P. Dharupaneedi, S. K. Nataraj, M. Nadagouda, K. R. Reddy, S. S. Shukla and T. M. Aminabhavi, *Sep. Purif. Technol.*, 2019, **210**, 850–866.

2 N. Mpongwana and S. Rathilal, A review of the techno-economic feasibility of nanoparticle application for wastewater treatment, *Water*, 2022, **14**(10), 1550.

3 A. A. Aryee, R. Han and L. Qu, *J. Cleaner Prod.*, 2022, **368**, 133140.

4 R. Mahmoud, N. Safwat, M. Fathy, N. A. Mohamed, S. El-Dek, H. A. El-Banna, A. Farghali and F. I. Abo El-Ela, *Arabian J. Chem.*, 2022, **15**, 103646.

5 R. K. Mahmoud, M. Taha, A. Zaher and R. M. Amin, *Sci. Rep.*, 2021, **11**, 21365.

6 L. Iezzi, G. Vilardi, G. Saviano and M. Stoller, *Chem. Eng. J.*, 2022, **449**, 137864.

7 V. Acevedo-García, E. Rosales, A. Puga, M. Pazos and M. A. Sanromán, *Sep. Purif. Technol.*, 2020, **242**, 116796.

8 A. V. Baskar, N. Bolan, S. A. Hoang, P. Sooriyakumar, M. Kumar, L. Singh, T. Jasemizad, L. P. Padhye, G. Singh, A. Vinu, B. Sarkar, M. B. Kirkham, J. Rinklebe, S. Wang, H. Wang, R. Balasubramanian and K. H. M. Siddique, *Sci. Total Environ.*, 2022, **822**, 153555.

9 M. S. Alias, S. K. Kamarudin, A. M. Zainoodin and M. S. Masdar, *Int. J. Hydrogen Energy*, 2020, **45**, 19620–19641.

10 L. Yaqoob, T. Noor and N. Iqbal, *Int. J. Energy Res.*, 2021, **45**, 6550–6583.

11 G. Rambabu, S. D. Bhat and F. M. L. Figueiredo, *Nanomaterials*, 2019, **9**, 1292.

12 A. Kaur, G. Kaur, P. P. Singh and S. Kaushal, *Int. J. Hydrogen Energy*, 2021, **46**, 15820–15849.

13 E. E. Abdel-Hady, R. Mahmoud, S. H. M. Hafez and H. F. M. Mohamed, *J. Mater. Res. Technol.*, 2022, **17**, 1922–1941.

14 R. Mahmoud, H. F. M. Mohamed, S. H. M. Hafez, Y. M. Gadelhak and E. E. Abdel-Hady, *Sci. Rep.*, 2022, **12**, 1–14.

15 W. Kamal, R. Mahmoud, A. E. Allah, A. Abdelwahab, M. Taha and A. A. Farghali, *Chem. Eng. Res. Des.*, 2022, **188**, 249–264.

16 P. Koehler, D. Tacke and O. A. Cornely, *Mycoses*, 2014, **57**, 323–335.

17 E. J. C. Goldstein, *Clin. Infect. Dis.*, 1992, **14**, 633–640.

18 A. Gürses, Ç. Doğar, M. Yalçın, M. Açıkyıldız, R. Bayrak and S. Karaca, *J. Hazard. Mater.*, 2006, **131**, 217–228.

19 S. Senthilkumaar, P. R. Varadarajan, K. Porkodi and C. V. Subbhuraam, *J. Colloid Interface Sci.*, 2005, **284**, 78–82.

20 W. Rudzinski and W. Plazinski, *Environ. Sci. Technol.*, 2008, **42**, 2470–2475.

21 M. Avrami, *J. Chem. Phys.*, 1941, **9**, 177–184.

22 V. Sarin, T. S. Singh and K. K. Pant, *Bioresour. Technol.*, 2006, **97**, 1986–1993.

23 F. Hadacek and H. Greger, *Phytochem. Anal.*, 2000, **11**, 137–147.

24 M. C. A. Leite, A. P. De Brito Bezerra, J. P. De Sousa, F. Q. S. Guerra and E. De Oliveira Lima, Evaluation of antifungal activity and mechanism of action of citral against Candida albicans, *J. Evidence-Based Complementary Altern. Med.*, 2014, **2014**, 1–9.

25 A. Espinel-Ingroff, V. Chaturvedi, A. Fothergill and M. G. Rinaldi, *J. Clin. Microbiol.*, 2002, **40**, 3776–3781.

26 P. Wayne, CLSI Document M27-A3 and Supplement S, 2008, vol. 3, pp. 6–12.

27 D. Kalemba and A. Kunicka, *Curr. Med. Chem.*, 2003, **10**, 813–829.

28 G. C. De Souza, A. P. S. Haas, G. L. Von Poser, E. E. S. Schapoval and E. Elisabetsky, *J. Ethnopharmacol.*, 2004, **90**, 135–143.

29 Y. A. Jeff-Agboola, A. K. Onifade, B. J. Akinyele and I. B. Osho, *J. Med. Plants Res.*, 2012, **6**, 4048–4056.

30 N. Boukmouche, N. Azzouz, L. Bouchama, J. P. Chopart and Y. Bouznit, *Arabian J. Chem.*, 2014, **7**, 347–354.

31 O. G. Hussein, K. Abdou, W. A. Moselhy and R. Mahmoud, *Appl. Clay Sci.*, 2023, **231**, 106724.

32 G. Y. Abo El-Reesh, A. A. Farghali, M. Taha and R. K. Mahmoud, *Sci. Rep.*, 2020, **10**, 587.

33 R. Nimal, R. Yahya, A. Shah, M. A. Khan, M. A. Zia and I. Shah, *Nanomaterials*, 2022, **12**, 1–12.

34 Youdhestar, F. K. Mahar, G. Das, A. Tajammul, F. Ahmed, M. Khatri, S. Khan and Z. Khatri, Fabrication of Ceftriaxone-Loaded Cellulose Acetate and Polyvinyl Alcohol Nanofibers and Their Antibacterial Evaluation, *Antibiotics*, 2022, **11**, 352.

35 F. A. H. Al-foraty, Q. M. Al-obaidy and A. A. H. Al, *Sci. J. Med. Res.*, 2022, **6**, 7–16.

36 P. Manimekalai, R. Dhanalakshmi and R. Manavalan, *Int. J. Appl. Pharm.*, 2017, **9**, 10–15.

37 M. B. Abd Elhaleem, A. A. Farghali, A. A. G. El-Shahawy, F. I. Abo El-Ela, Z. E. Eldine and R. K. Mahmoud, *RSC Adv.*, 2020, **10**, 13196–13214.

38 H. M. Owens and A. K. Dash, *Profiles of Drug Substances, Excipients and Related Methodology*, 2003, pp. 21–57.

39 K. K. Abbas, A. M. H. AbdulkadhimAl-Ghaban and E. H. Rdewi, *J. Environ. Chem. Eng.*, 2022, **10**, 108111.

40 V. P. Nguyen, K. T. T. Nguyen, L. T. Ton, D. T. Nguyen, K. Q. Nguyen, M. T. Vu and H. N. Tran, *J. Nanomater.*, 2020, **2020**, 1–11.

41 L. Fang, W. Li, H. Chen, F. Xiao, L. Huang, P. E. Holm, H. C. B. Hansen and D. Wang, *RSC Adv.*, 2015, **5**, 18866–18874.

42 C. V. Luengo, M. A. Volpe and M. J. Avena, *J. Environ. Chem. Eng.*, 2017, **5**, 4656–4662.

43 R. Rojas Delgado, C. P. De Pauli, C. B. Carrasco and M. J. Avena, *Appl. Clay Sci.*, 2008, **40**, 27–37.

44 R. Rojas Delgado, M. Arandigoyen Vidaurre, C. P. De Pauli, M. A. Ulibarri and M. J. Avena, *J. Colloid Interface Sci.*, 2004, **280**, 431–441.

45 A. D. Ado, M. Muhammad, A. D. Mahmud and T. Oyegoke, *Adsorption*, 2019, **100**, 1.

46 I. Langmuir, *J. Am. Chem. Soc.*, 1918, **40**, 1361–1403.

47 B. Nagy, C. Mânzatu, A. Măicăneanu, C. Indolean, L. Barbu-Tudoran and C. Majdik, *Arabian J. Chem.*, 2017, **10**, S3569–S3579.

48 M. M. Dubinin, *Chem. Rev.*, 1960, **60**, 235–241.

49 R. Sips, *J. Chem. Phys.*, 1948, **16**, 490–495.

50 O. Redlich and D. L. Peterson, *J. Phys. Chem.*, 1959, **63**, 1024.

51 P. B. Vilela, A. Dalalibera, E. C. Duminelli, V. A. Becegato and A. T. Paulino, *Environ. Sci. Pollut. Res.*, 2019, **26**, 28481–28489.

52 J. Toth, *Acta Chim. Hung.*, 1971, **69**, 311–328.

53 M. Baudu, Etude des interactions solutes-fibres de charbon actif: applications et regeneration, PhD diss., 1990.

54 M. Matouq, N. Jildeh, M. Qtaishat, M. Hindiyeh and M. Q. Al Syouf, *J. Environ. Chem. Eng.*, 2015, **3**, 775–784.

55 F. Y. Al Jaberi, S. M. Jabbar and N. M. Jabbar, *AIP Conf. Proc.*, 2020, 020041.

56 *AgriMetSoft*, 2019.

57 A. W. Marczewski, *Appl. Surf. Sci.*, 2010, **256**, 5145–5152.

58 G. Y. A. El-Reesh, A. A. Farghali, M. Taha and R. K. Mahmoud, *Sci. Rep.*, 2020, **10**, 1–20.

59 V. P. Vinod and T. S. Anirudhan, *J. Chem. Technol. Biotechnol.*, 2002, **77**, 92–101.

60 M. Horsfall Jr and A. I. Spiff, *Electron. J. Biotechnol.*, 2005, **8**(2), 43–50.

61 H. Rashidi Nodeh and H. Sereshti, *RSC Adv.*, 2016, **6**, 89953–89965.

62 Y. GadelHak, E. Salama, S. Abd-El Tawab, E. Mouhmed, D. Alkhalifah, W. Hozzein, M. Mohaseb, R. Mahmoud and R. Amin, *ACS Omega*, 2022, **7**(48), 44103–44115.

63 M. E. Mahmoud, A. M. El-Ghanam, R. H. A. Mohamed and S. R. Saad, *Mater. Sci. Eng., C*, 2020, **108**, 110199.

64 S. bozorginia, J. Jaafari, K. Taghavi, S. D. Ashrafi, E. Roohbakhsh and D. Naghipour, *Int. J. Environ. Anal. Chem.*, 2021, 1–15.

65 X. Shi, A. Karachi, M. Hosseini, M. S. Yazd, H. Kamyab, M. Ebrahimi and Z. Parsaee, *Ultrason. Sonochem.*, 2020, **68**, 104460.

66 M. Y. Badi, A. Azari, H. Pasalari, A. Esrafili and M. Farzadkia, *J. Mol. Liq.*, 2018, **261**, 146–154.

67 E. E. Abdel-Hady, R. Mahmoud, S. H. M. Hafez and H. F. M. Mohamed, *J. Mater. Res. Technol.*, 2022, **17**, 1922–1941.

68 G. M. Abdelrazek, M. M. EL-Deeb, A. A. Farghali, A. F. Pérez-Cadenas and A. Abdelwahab, *Materials*, 2021, **14**, 5271.

69 K. Patil, P. Babar, D. M. Lee, V. Karade, E. Jo, S. Korade and J. H. Kim, *Sustainable Energy Fuels*, 2020, **4**, 5254–5263.

70 S. Gamil, M. Antuch, I. T. Zedan and W. M. A. El Rouby, *Colloids Surf., A*, 2020, **602**, 125067.

71 S. Gamil, W. M. A. El Rouby, M. Antuch and I. T. Zedan, *RSC Adv.*, 2019, **9**, 13503–13514.

72 P. Krawczyk, T. Rozmanowski and M. Frankowski, *Catal. Lett.*, 2019, **149**, 2307–2316.

73 Y. Wang, D. Zhang, W. Peng, L. Liu and M. Li, *Electrochim. Acta*, 2011, **56**, 5754–5758.

74 K. Patil, P. Babar, D. M. Lee, V. Karade, E. Jo, S. Korade and J. H. Kim, *Sustainable Energy Fuels*, 2020, **4**, 5254–5263.

75 J. A. Cruz-Navarro, L. H. Mendoza-Huizar, V. Salazar-Pereda, J. Á. Cobos-Murcia, R. Colorado-Peralta and G. A. Álvarez-Romero, *Inorg. Chim. Acta*, 2021, **520**, 120293.

76 M. A. Aguilar-Méndez, E. S. Martín-Martínez, L. Ortega-Arroyo, G. Cobián-Portillo and E. Sánchez-Espíndola, *J. Nanopart. Res.*, 2011, **13**, 2525–2532.

77 G. Petrikkos, A. Skiada, O. Lortholary, E. Roilides, T. J. Walsh and D. P. Kontoyiannis, *Clin. Infect. Dis.*, 2012, **54**, S23–S34.

78 U. Binder, E. Maurer and C. Lass-Flörl, *Clin. Microbiol. Infect.*, 2014, **20**, 60–66.

79 R. Kronen, S. Y. Liang, G. Bochicchio, K. Bochicchio, W. G. Powderly and A. Spec, *Int. J. Infect. Dis.*, 2017, **62**, 102–111.

80 M. E. Arnáiz-García, D. Alonso-Peña, M. del Carmen González-Vela, J. D. García-Palomo, J. R. Sanz-Giménez-Rico and A. M. Arnáiz-García, *Journal of Plastic, Reconstructive & Aesthetic Surgery*, 2009, **62**, e434–e441.

81 H. Kaur, A. Ghosh, S. M. Rudramurthy and A. Chakrabarti, *Mycoses*, 2018, **61**, 898–908.

82 C. Vivanco, K. Paola, and L. Alejandra, G. Cáceres, Revisión bibliográfica narrativa: mortalidad y complicaciones de mucormicosis en zonas rino-orbital y rinocerebral en pacientes inmunocomprometidos con leucemia, PhD thesis, 2021.

83 D. J. Frost, K. I. M. D. Brandt, D. Cugier and R. Goldman, *J. Antibiot.*, 1995, **48**, 306–310.

84 L. Svetaz, M. B. Agüero, S. Alvarez, L. Luna, G. Feresin, M. Derita, A. Tapia and S. Zacchino, *Planta Med.*, 2007, **73**, 1074–1080.

85 P. A. Wayne, CLSI document M27-A2.

86 J. Awassa, D. Cornu, S. Soulé, C. Carteret, C. Ruby and S. El-Kirat-Chatel, *Appl. Clay Sci.*, 2022, **216**, 106369.

87 F. Peng, D. Wang, D. Zhang, H. Cao and X. Liu, *Appl. Clay Sci.*, 2018, **165**, 179–187.

88 M. Lobo-Sánchez, G. Nájera-Meléndez, G. Luna, V. Segura-Pérez, J. A. Rivera and G. Fetter, *Appl. Clay Sci.*, 2018, **153**, 61–69.

89 Y. Qiao, Q. Li, H. Chi, M. Li, Y. Lv, S. Feng, R. Zhu and K. Li, *Appl. Clay Sci.*, 2018, **163**, 119–128.

90 R. Saravanan, M. M. Khan, V. K. Gupta, E. Mosquera, F. Gracia, V. Narayanan and A. Stephen, *RSC Adv.*, 2015, **5**, 34645–34651.

91 M. G. Nair, M. Nirmala, K. Rekha and A. Anukaliani, *Mater. Lett.*, 2011, **65**, 1797–1800.

92 D. Wang, N. Ge, S. Qian, J. Li, Y. Qiao and X. Liu, *RSC Adv.*, 2015, **5**, 106848–106859.

93 Q. Li, H. Tang, Y.-Z. Li, M. Wang, L.-F. Wang and C.-G. Xia, *J. Inorg. Biochem.*, 2000, **78**, 167–174.

94 N. J. Hallab, C. Vermes, C. Messina, K. A. Roebuck, T. T. Glant and J. J. Jacobs, *J. Biomed. Mater. Res.*, 2002, **60**, 420–433.

95 M. T. Qamar, M. Aslam, Z. A. Rehan, M. T. Soomro, J. M. Basahi, I. M. I. Ismail, T. Almeelbi and A. Hameed, *Appl. Catal., B*, 2017, **201**, 105–118.

96 G. B. Bagihalli, P. G. Avaji, S. A. Patil and P. S. Badami, *Eur. J. Med. Chem.*, 2008, **43**, 2639–2649.

97 W.-L. Du, S.-S. Niu, Y.-L. Xu, Z.-R. Xu and C.-L. Fan, *Carbohydr. Polym.*, 2009, **75**, 385–389.

98 A. Mukherjee, I. Mohammed Sadiq, T. C. Prathna and N. Chandrasekaran, *Science against Microbial Pathogens: Communicating Current Research and Technological Advances*, 2011, **1**, 245–251.

99 A. Sirelkhatim, S. Mahmud, A. Seeni, N. H. M. Kaus, L. C. Ann, S. K. M. Bakhori, H. Hasan and D. Mohamad, *Nano-Micro Lett.*, 2015, **7**, 219–242.

100 S. H. Kim, S.-Y. Kwak, B.-H. Sohn and T. H. Park, *J. Membr. Sci.*, 2003, **211**, 157–165.

101 C. Mousty and V. Prévot, *Anal. Bioanal. Chem.*, 2013, **405**, 3513–3523.

102 R. Cortivo, V. Vindigni, L. Iacobellis, G. Abatangelo, P. Pinton and B. Zavan, *Nanomedicine*, 2010, **5**, 641–656.

103 E. Maikranz, C. Spengler, N. Thewes, A. Thewes, F. Nolle, P. Jung, M. Bischoff, L. Santen and K. Jacobs, *Nanoscale*, 2020, **12**, 19267–19275.

104 S. Hwangbo, H. Jeong, J. Heo, X. Lin, Y. Kim, M. Chang and J. Hong, *React. Funct. Polym.*, 2016, **102**, 27–32.

105 X. Ji, P. Liu, J. Tang, C. Wan, Y. Yan, Z. Zhao and D. Zhao, *Trans. Nonferrous Met. Soc. China*, 2021, **31**, 3821–3830.

106 K. Yang, J. Shi, L. Wang, Y. Chen, C. Liang, L. Yang and L.-N. Wang, *J. Mater. Sci. Technol.*, 2022, **99**, 82–100.